

**Stochastic Method and Convex Optimization in Inverse Electromagnetic  
Scattering**

BY

YANGQING LIU

B.E., Hebei University of Engineering, 2011  
M.E.E., University of Alaska Fairbanks, 2014

THESIS

Submitted as partial fulfillment of the requirements  
for the degree of Doctor of Philosophy in Electrical and Computer Engineering  
in the Graduate College of the  
University of Illinois Chicago, 2022

Chicago, Illinois

Defense Committee:

Danilo Erricolo, Chair and Advisor  
Pai-Yen Chen  
Shuo Han  
Daniela Tuninetti  
Piergiorgio L. E. Uslenghi  
Ilaria Catapano, IREA-CNR  
Jaideva C. Goswami, National Oilwell Varco

Copyright by

Yangqing Liu

2022

*to all those who have helped me*

## ACKNOWLEDGMENTS

The author is deeply grateful to Danilo Erricolo for his constant support, guidance, and kindness, Vincent Adiutori, Wolfgang-Martin Boerner, Ilaria Catapano, Pai-Yen Chen, Jaideva C. Goswami, Shuo Han, Alexander Heifetz, Chuck La Chance, Sharad Laxpati, Dia Mason, Francesco Soldovieri, Daniela Tuninetti, and Piergiorgio L. E. Uslenghi for inspiring discussions, John Eichelberger, Wenyu Gong, Joe Hawkins, Carol Holz, Jon Klein, Hsin-Hui Yen, and Jinghui Zheng, who made it possible to start this work.

YL

## CONTRIBUTION OF AUTHORS

This dissertation is a compilation of the collaboration among my advisor Professor Danilo Erricolo, my coauthors Professor Shuo Han and Dr. Francesco Soldovieri, and me. Our contributions to two-dimensional inverse scattering problems are: in Chapter 3, a two-step combination of the classic Born iterative method and the well-known genetic algorithm [1] and a new application of Monte Carlo Markov Chain for Bayesian inference of unknown permittivity given the electric field [2]; in Chapter 4, a new approximation using convex optimization for electromagnetic inverse scattering [3].

Professor Danilo Erricolo was the lead investigator throughout all my work. Dr. Francesco Soldovieri provided feedback and edited the manuscripts of [1,3]. Professor Shuo Han proposed the research idea of approximating the nonlinear problem using convex optimization, chose the MATLAB packages (CVX for disciplined convex programming and TFOCS for first-order conic solvers), and edited the manuscript of [3]. Dr. Jaideva C. Goswami suggested projecting the permittivity in the space domain to the wavelet domain in [3]. The measured electric field data used in [3] were collected by Dr. Vittorio Picco and Dr. Tadahiro Negishi. I was responsible for the research ideas in [1,2] and developing codes for all numerical data and results.

## TABLE OF CONTENTS

<u>CHAPTER</u>	<u>PAGE</u>
<b>1 INTRODUCTION</b> . . . . .	1
1.1 Applications: from the Moon to the Earth . . . . .	2
1.2 Projection-Slice Theorem and Tomography . . . . .	4
1.3 Summary of Chapters . . . . .	6
 <b>2 FUNDAMENTALS OF ELECTROMAGNETIC INVERSE SCATTERING</b> . . . . .	 8
2.1 Problem Statement . . . . .	8
2.1.1 Two-Dimensional Electromagnetic Scattering . . . . .	9
2.1.2 Scattering Problem . . . . .	12
2.1.3 Inverse Scattering Problem . . . . .	13
2.2 Previous Solutions . . . . .	15
2.2.1 Approximations . . . . .	16
2.2.2 From Nonlinear to Linear: Born Related Methods . . . . .	17
2.2.3 Method of Moment - Discretization of EFIE . . . . .	20
2.2.4 Optimization and Parameter Estimation . . . . .	23
2.2.4.1 Deterministic Regularizations . . . . .	24
2.2.4.2 Stochastic Evolutionary Optimization Algorithms . . . . .	25
2.3 Roadmap . . . . .	27
 <b>3 STOCHASTIC METHODS AND BAYESIAN INFERENCE</b> . . . . .	 28
3.1 A Hybrid of BIM and GA . . . . .	29
3.1.1 Numerical Results . . . . .	31
3.1.1.1 A Homogeneous Scatterer: Permittivity of 1.6 . . . . .	33
3.1.1.2 A Layered Circular Cylinder . . . . .	34
3.1.2 Discussion . . . . .	34
3.2 Bayesian Inference . . . . .	39
3.2.1 Numerical Results . . . . .	42
3.2.2 Discussion . . . . .	47
 <b>4 CONVEX OPTIMIZATION</b> . . . . .	 49
4.1 Theory . . . . .	51
4.1.1 Approximation with Convex Optimization . . . . .	53
4.1.2 Linear Inversions in the Wavelet Domain . . . . .	56
4.2 Numerical Results . . . . .	60
4.2.1 A Homogeneous Circular Cylinder: Lossless and Lossy . . . . .	60
4.2.1.1 A Lossless Homogeneous Cylinder: $\epsilon = 11$ . . . . .	60

## TABLE OF CONTENTS (Continued)

<u>CHAPTER</u>		<u>PAGE</u>
4.2.1.2	A Lossy Homogeneous Cylinder: $\epsilon = 2 - 1j$ . . . . .	65
4.2.2	An Inhomogeneous Circular Cylinder . . . . .	66
4.2.2.1	A Sine Shape Distribution . . . . .	66
4.2.2.2	A Layered Cylinder . . . . .	68
4.2.3	Detection of Shape and Dielectric Properties . . . . .	70
4.2.3.1	L-shaped Plexiglass . . . . .	70
4.2.3.2	Two High Density Polyethylene Cylinders from Measurement . . . . .	71
4.3	Discussion . . . . .	73
<b>5</b>	<b>CONCLUDING REMARKS</b> . . . . .	<b>74</b>
5.1	Summary . . . . .	74
5.2	Future Directions . . . . .	75
	<b>APPENDICES</b> . . . . .	<b>77</b>
	<b>Appendix A</b> . . . . .	<b>78</b>
	<b>Appendix B</b> . . . . .	<b>85</b>
	<b>Appendix C</b> . . . . .	<b>89</b>
	<b>CITED LITERATURE</b> . . . . .	<b>91</b>
	<b>VITA</b> . . . . .	<b>100</b>

## LIST OF TABLES

<u>TABLE</u>		<u>PAGE</u>
I	MEAN AND RMS DEVIATION FOR FOUR METHODS . . . . .	33
II	KEY SYMBOLS . . . . .	59

## LIST OF FIGURES

<u>FIGURE</u>		<u>PAGE</u>
1	A tomographic configuration . . . . .	10
2	The tomographic configuration for inferring permittivity in: (a) a continuous form; (b) a discrete form. . . . .	21
3	Roadmap . . . . .	27
4	BIM reconstructed results for the permittivity within a cylinder, $\epsilon = 1.6$ : (a) ART; (b) CG; (c) ART-GA hybrid; (d) CG-GA hybrid. . . . .	35
5	Cross sectional view of reconstructed relative permittivity along $Y = 0$ for the homogeneous cylinder of $\epsilon = 1.6$ . . . . .	36
6	BIM reconstructed results for the permittivity within a layered cylinder, outer $\epsilon = 4$ , inner $\epsilon = 2$ : (a) ART; (b) CG; (c) ART-GA hybrid; (d) CG-GA hybrid. . . . .	37
7	Cross sectional view of reconstructed relative permittivity along $Y = 0$ for the layered cylinder with the outer layer of $\epsilon = 4$ and the inner layer of $\epsilon = 2$ . . . . .	38
8	BIM reconstructed results for the permittivity within a cylinder, $\epsilon = 11$ : (a) real part; (b) conductivity. . . . .	44
9	Reconstructed results for real part of the permittivity: (a) MCMC results within the cylinder; (b) slice comparisons along the horizontal axis. . . . .	46
10	Comparison of scattered fields from the forward model. Left axis: error percentage of amplitude. Right axis: phase. . . . .	48
11	Electric field relative error within the cylinder with $\epsilon = 11$ : (a) $\Re\delta^{\text{BIM}}$ ; (b) $\Re\delta^{\text{CVX}}$ ; (c) $\Im\delta^{\text{BIM}}$ ; (d) $\Im\delta^{\text{CVX}}$ . The red dot at $(0, 0.075\lambda)$ shows the location of the transmitter. Results on the same row share the colorbar on the right. . . . .	62
12	Permittivity reconstruction of the cylinder with $\epsilon = 11$ by: (a) BIM; (b) CVX-TFOCS. Results share the colorbar on the right. . . . .	63

## LIST OF FIGURES (Continued)

<u>FIGURE</u>		<u>PAGE</u>
13	Real part of permittivity reconstructed along $y = 0$ by BIM and CVX-TFOCS for a circular cylinder with permittivity 11 with varying radius, $\lambda/20$ , $\lambda/8$ , $\lambda/4$ , and $\lambda/2$ . . . . .	64
14	Permittivity reconstruction of the cylinder $\epsilon = 2 - 1j$ , i.e. $\sigma = 0.0556$ : (a) real part; (b) conductivity. . . . .	65
15	Relative error of electric field for the sine-shaped distribution: (a) $\Re\delta^{\text{Noiseless}}$ ; (b) $\Re\delta^{30 \text{ dB}}$ ; (c) $\Im\delta^{\text{Noiseless}}$ ; (d) $\Im\delta^{30 \text{ dB}}$ . The red dot at $(0, 0.375\lambda)$ shows the location of the transmitter. Results on the same row share the colorbar on the right. . . . .	67
16	Reconstructed real part of permittivity within a sine-shaped permittivity distribution with maximum $\epsilon = 3$ at $(0, 0)$ and the minimum of 1 at the edge: (a) noiseless; (b) 30 dB SNR. . . . .	68
17	Real part of permittivity within a sine-shaped permittivity distribution with maximum $\epsilon = 3$ at $(0, 0)$ and the minimum of 1 at the edge: (a) actual; (b) reconstructed with a 20 dB SNR. Results share the colorbar on the right. . . . .	69
18	Reconstructed permittivity of a layered cylinder, the red line indicates the actual boundary between the outer layer with $\epsilon = 4$ and the inner layer with $\epsilon = 2$ : (a) noiseless; (b) 20dB SNR. . . . .	70
19	Reconstructed permittivity of an L-shaped plexiglass with $\epsilon = 2.6$ : (a) noiseless; (b) 20dB SNR. . . . .	71
20	Reconstructed permittivity of two HDPE cylinders with $\epsilon = 2.26$ : (a) quadratic model; (b) CVX-TFOCS. The red circles indicate the contour of the original cylinders. Results share the colorbar on the right. . . . .	72
21	Relative permittivity distribution: (a) a circular shell: the outer radius is $0.3 \lambda$ and the inner radius is $0.25 \lambda$ ; (b) a semi-circular shell. . . . .	87
22	MoM solver results for Figure 21a: (a) electric field in the shell along the radius of $0.275\lambda$ ; (b) echo width with a plane wave incident; (c) echo width with a line source incident. MoM solver results for Figure 21b: (d) echo width with a plane wave incident. . . . .	88

## LIST OF ABBREVIATIONS

ADC	Analog-to-Digital Converter
ART	Algebraic Reconstruction Technique
AWGN	Additive White Gaussian Noise
BIM	Born Iterative Method
CG	Conjugate Gradient
DBIM	Distorted Born Iterative Method
EFIE	Electric Field Integral Equation
GA	Genetic Algorithm
GPR	Ground Penetrating Radar
HF	High Frequency
LASSO	Least Absolute Shrinkage and Selection Operator
MCMC	Monte Carlo Markov Chain
PEC	Perfectly Electric Conductor
RADAR	Radio Detection and Ranging
RF	Radio Frequency
RX	Receiver
SNR	Signal-to-Noise Ratio

## LIST OF ABBREVIATIONS (Continued)

SVD	Singular Value Decomposition
TFOCS	Templates for First-Order Conic Solvers
TM	Transverse Magnetic
TX	Transmitter

## SUMMARY

Electromagnetic inverse scattering problems arise in many engineering applications. The electromagnetic scattering phenomenon is characterized by the electric field integral equation. In inverse problems, this integral equation describes the nonlinear relationship between the unknown complex permittivity distribution in an investigation domain and the observable scattered fields. Nonlinear inverse scattering problems can be approximated to be linear by the Born approximation and iteratively solved by Newton's method with regularizations. Or they can be approached by minimizing a cost function that consists of norms with optimization techniques.

First, we attempt the joint exploitation of the deterministic linear inversion and global optimization strategies. The first step is based on the Born iterative method (BIM) enhanced by regularization techniques, Algebraic Reconstruction Technique (ART) and Conjugate Gradient (CG). In the second step of the overall strategy, a stochastic global optimization approach, the genetic algorithm (GA), is carried out. In this way, we will benefit from the results from previous regularization schemes as the initial population. Numerical results are presented with reference to the permittivity reconstructions in the case of a homogeneous cylinder and an inhomogeneous layered cylinder.

Second, we propose a new application of Monte Carlo Markov Chain (MCMC) methods to infer permittivity values. Instead of using regularizations to uncover the best fit of permittivity, we estimate the conditional mean of the unknown permittivity given scattered field data. The

## SUMMARY (Continued)

conditional mean estimates not only incorporate prior knowledge from results obtained by BIM, but also avoid the nonlinearity by computing the linear forward model. For a homogeneous cylinder with the relative permittivity of 11, numerical results of BIM are slightly improved by this Bayesian inference approach.

Last, we consider the inverse scattering problem from a convex optimization perspective. The first step approximates the inverse scattering as a convex optimization problem and provides an estimation of the internal electric field inside the domain under investigation without a priori knowledge or tuning parameters. In the second step, the previously estimated total field is used to reconstruct the unknown contrast permittivity, which is represented by a superposition of level-1 Haar wavelet transform basis functions. Subject to  $\ell_1$ -norm constraints of the wavelet coefficients, a LASSO problem that searches for the global minimum of the  $\ell_2$ -norm residual is exploited by accounting for the sparsity of the wavelet-based permittivity representation. Numerical results are presented to assess the effectiveness of the proposed formulation against objects with relatively small electric size. Finally, the approach is validated against experimental data.

## CHAPTER 1

### INTRODUCTION

“We may find illustrations of the highest doctrines of science in games and gymnastics, in travelling by land and by water, in storms of the air and of the sea, and wherever there is matter in motion.”

---

James Clerk Maxwell

Consider a black box. While pondering what is inside, one might excite this system with known stimuli, observe responses, and characterize its properties. This process describes an inverse problem, which starts from results and looks for causes.

In electromagnetic inverse scattering problems, we aim to characterize electromagnetic properties of the interior of the black box. As the stimulus, the incident electromagnetic field illuminates the black box, i.e. the object under investigation, which then scatters the incident field back as the response. Not only does such a stimulus/response pair can be observed, but it also belongs in the realm of electromagnetics governed by the Maxwell equations. Derived from the Maxwell equations, in a physical sense, an electric field integral equation (EFIE) formulates the stimulus/response of a black box; it describes a scattering problem in unbounded media. In a mathematical sense, the EFIE is in the form of Fredholm equations. Therefore, to solve inverse scattering problem, EFIEs are the key element.

In this chapter, we will walk through the history, review applications of inverse problems, and introduce previous techniques solving inverse scattering problems.

## 1.1 Applications: from the Moon to the Earth

Let us visit diverse fields where inverse problems emerge before diving into more mathematical details.

Before Neil Armstrong's "one giant leap for mankind" in 1969, radio engineers had sent electromagnetic waves over a wide range of frequencies to detect the Moon: the reflected wave from the Moon was received on the Earth for the first time in 1946 [4]; relative dielectric constant and roughness of the center of the lunar disk were predicted in 1963 [5] and confirmed by Surveyor and Apollo data [6]. The inverse problem scheme here is to infer the Moon's landscape (cause) from observed echoes (result). The frequency, power level, polarization, time delay, and other information of the echo led us to the Moon's property.

Why human deploy electromagnetic waves for space mission? 1. an electromagnetic wave is not a mechanical wave, therefore it can travel in vacuum; 2. we cannot find anything traveling faster than light, and light is an electromagnetic radiation from 430 THz to 750 THz. As Maxwell wrote in 1865 [7], "This velocity is so nearly that of light, that it seems we have strong reason to conclude that light itself (including radiant heat, and other radiations if any) is an electromagnetic disturbance in the form of waves propagated through the electromagnetic field according to electromagnetic laws."

An electromagnetic echo might run into many accidents during its trip in space; a line of sight model with speed of light is too simplified, just like a solution to a low milk production

problem works only with spherical cows in a vacuum. First, as William Gilbert pointed out in 1600, the Earth has a magnetic field; so the echo path in the magnetosphere, which is dominated by the Earth's magnetic field, is impacted. Especially, the Earth's magnetic field can be temporarily disturbed in a geomagnetic storm, which brings a surge in the flux of charged particles from the Sun. Besides, the electromagnetic radiation and emission of energetic particles (solar wind) from the Sun [8] ionize the Earth's upper atmosphere, and the ionized molecules of hydrogen, helium, and oxygen releasing free electrons turn into plasma. Since cold plasmas vary the refractive index for electromagnetic wave propagation as described as the Appleton–Lassen dispersion relationship [9], they bend the echo path in addition to the Faraday rotation in the Earth's ionosphere. Some of the bended electromagnetic waves can be totally reflected in the ionosphere before reaching to the Moon. Last but not least, even if the wave traveled back to the Earth atmosphere, common energy burst by lightning generates a wide frequency range of electromagnetic waves. These radiations produced by the lightning electrostatic discharge can propagate in the atmosphere, bounce back and forth between the Earth and the atmosphere/ionosphere boundary (both are good conductors), and therefore might travel across hemispheres [10].

Scientists had made tremendous amount of effort obtaining routine electron density information in space plasmas over large geographic regions at altitudes above the topside ionosphere. In the past, ground-based ionosondes sent High Frequency (HF) pulses and recorded the echo travel time with respect to frequency. Space-borne relaxation can excite local space plasma resonance to determine electron density and newer magnetospheric incorporates digital signal processing

techniques over long propagation distances. Again, characteristics of the space plasma at those remote reflection points as well as electron and ion density profiles along the echo path can “be derived from measurements of the echo amplitude, phase, delay time, frequency, polarization, Doppler shift, and echo direction” [11].

There are many other factors that determine the electromagnetic propagation, such as the atmospheric attenuation and refraction. However, we can generalize applications of electromagnetic waves mentioned as remote sensing in space with RADAR techniques [12]. As a detection system, RADAR uses electromagnetic waves to determine target’s location, velocity, or physical properties.

A RADAR consists of antennas, transmitters, receivers, excitors, and signal processors subsystems. Other than the hardware that physically transmits and receives electromagnetic waves, the signal processor is responsible for extracting detection and measurement results by implementing digital signal processing algorithms. If antennas, switch duplexers, low noise amplifiers, local oscillators, ADCs are the body of a RADAR, digital signal processing is the brain. In the next section, we will review some fundamental concepts in digital signal processing for inverse problems.

## **1.2 Projection-Slice Theorem and Tomography**

In digital signal processing, inverse problems can be generally sketched as determining the input from corresponding known output; common examples include noise removal, deconvolution, signal extrapolation, and reconstruction of signals from their projections [13]. In this context, a projection is a mapping of an  $N$  dimensional set to an  $N - 1$  dimensional one by in-

tegrating the  $N$  dimensional set along a particular direction. Therefore, a 2D object scanned by X-rays has 1D projections, or geologic objects illuminated by acoustic beams from one borehole has projections measured along another borehole.

Now when we look at an  $N$  dimensional signal  $f(\mathbf{x})$  projected onto the  $N - 1$  dimensional space,  $(x_1, \dots, x_{i-1}, x_{i+1}, \dots, x_N)$ , the projection along the  $i$ -th dimension is

$$p_{x_i} = \int_{-\infty}^{\infty} f(\mathbf{x}) dx_i, \quad (1.1)$$

and its Fourier transform is

$$P_{\omega_i} = \int_{-\infty}^{\infty} \cdots \int_{-\infty}^{\infty} p_{x_i} \exp(-j(\omega_1 x_1 + \cdots + \omega_{i-1} x_{i-1} + \omega_{i+1} x_{i+1} + \cdots + \omega_N x_N)) dx_1 \cdots dx_{i-1} dx_{i+1} \cdots dx_N, \quad (1.2)$$

which is exactly a slice of the Fourier transform of  $f(\mathbf{x})$ ,  $F(\boldsymbol{\omega})$ , at  $\omega_i = 0$ . This is the remarkable projection-slice theorem firstly applied to signal reconstruction in [14].

Based on the projection-slice theorem, an  $N$  dimensional problem can be reduced to a sum of slices in  $N - 1$  dimension, which can also be reduced iteratively down to 2D problems. Therefore, any  $N$  dimensional problem can be solved by a set of 2D problems, and projections along all  $N - 1$  dimensions are not necessary. Let us restate the projection-slice theorem in 2D: the slice of the Fourier transform of a 2D function through the spectrum origin is the Fourier transform of this 2D function's 1D projection.

Even though we are dealing with 2D problems, in reality we cannot obtain infinite number of 1D projections. To estimate number of projections  $M$ , we assume that  $x(u_1, u_2)$  has a diameter  $d$  and resolution of reconstruction needed is  $r$ . From the sampling theorem, samples' space in the frequency domain  $\Omega$  is  $2\pi/d$ . If the sampling number  $M$  of the frequency domain in the projection-slice method has to satisfy  $M > \pi d/r$ . It's obvious that increasing the number of projections  $M$  would result in better resolution; the more the merrier!

The projection can be represented as the Radon transform [15], which is widely used in tomographic reconstruction [16] such as computed tomography (CT) scan and MRI. Tomography, from ancient Greek meaning “view by the slice”, images the internal structure of an object by sections with penetrating waves. Such an image revealing the internal structure of the object under investigation is a tomograph. Especially, when multi-illuminations are along a circular orbit, this is a tomographic configuration. For our inverse scattering problem, this is the exact setup we use numerically and experimentally. And we will start our journey in Chapter 2.

### **1.3 Summary of Chapters**

We focus on the two-dimensional electromagnetic inverse scattering problem for reconstructing the permittivity of the domain under investigation. Chapter 2 details fundamental theories for the problem statement and reviews some previous research endeavors. Chapter 3 introduces the mathematical background and present numerical results of stochastic methods: 1. a hybrid of a classic method with deterministic regularizations and genetic algorithms; 2. Bayesian inference with Monte Carlo Markov chains. Chapter 4 develops an approximation based on

convex optimization, and verifies the method with numerical and measured data. Chapter 5 concludes this work and proposes future directions.

## CHAPTER 2

### FUNDAMENTALS OF ELECTROMAGNETIC INVERSE SCATTERING

“Once a Vector, always a Vector.”

---

Oliver Heaviside

Besides the remote sensing and radar applications in Chapter 1, inverse problems explore causes from observations and arise in many practical areas; the electromagnetic and morphological properties of targets are estimated from the scattered field [17, 18]. There are many applications of inverse problems: for concrete specimens, from determining physical thickness [19] to nondestructive testing of concrete [20] to monitoring of dielectric permittivity in chemical alkali-silica reaction [21]; for below ground, from probing buried targets with ground penetrating radar (GPR) [22, 23] to tunnel detection [24, 25] to below ground close-in sensing [26] to irregular terrain investigation using RF tomography [27, 28], to oilfield exploration [29]; for medical purposes, from medical imaging with neural networks [30] to MRI [31].

This chapter reviews the theoretical background for forward and inverse electromagnetic scattering problems, introduces previous approaches and optimization techniques, and lays the foundation for Chapter 3 and Chapter 4.

#### **2.1 Problem Statement**

Inverse scattering problems are the reverse of the forward scattering problems. One shoots known incident waves to a box, then the game is between the box and the field scattered by it:

if you know the box, it is a forward problem; if you know the scattered field, an inverse one. What is the box in the context of electromagnetic scattering? Permittivity.

Another way to look at this is to think the incident field as the input, the box as the system function, and the scattered field as the output. With the known incident field, the inverse scattering problem wonders about what is inside a black box (system) from scattered field (output), while the forward problem looks for the output while knowing the system.

Even if our focus lies on the inverse scattering problem, introducing the forward one in the realm of inverse problems is more than a gesture of courtesy: the forward scattering problem strongly interacts with the solutions to the inverse problem. We will reveal that connection in this section, starting from general electromagnetic scattering phenomena.

### **2.1.1 Two-Dimensional Electromagnetic Scattering**

Before any equations kicking in, let us demonstrate the geometric setup of our problem in Figure 1. It is a tomographic configuration: the investigation domain in gray is surrounded by a red transmitter (TX) and blue receivers (RX) along a circle. While the investigation domain  $S$  is illuminated by only one transmitter each time, the scattered field is observed at all receivers; this is a multistatic measurement because there are multiple receivers. Once the transmitter is set at various locations (not at the same time), this is multi-illumination measurements. Therefore, multi-illumination and multistatic implementations are attained.

To construct a two-dimensional problem, we assume the investigation domain has an infinitely long cylindrical geometry and a homogeneous permittivity along  $\hat{z}$ ; this means the permittivity can only vary on the  $xy$ -plane, and thus it is not a function of  $z$ . Similarly, the

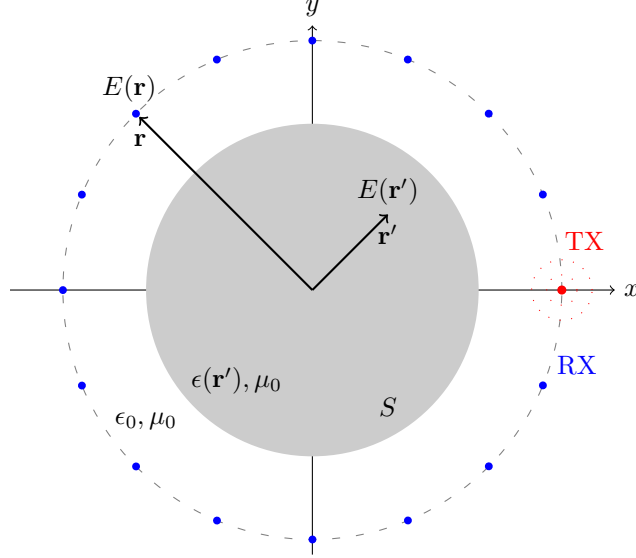


Figure 1: A tomographic configuration

incident field for a two-dimensional problem should be invariant along  $\hat{z}$ ; this can be achieved by an infinitely long electric line source aligned in the direction of  $\hat{z}$  with the transverse magnetic polarization, i.e.  $\text{TM}^z$ -mode. In free space (vacuum), such a source transmits the invariant incident field along  $\hat{z}$  expressed as

$$E_z^i = -\frac{k_0^2 I_e}{4\omega\epsilon_0} H_0^{(2)}(k_0 |\mathbf{r} - \mathbf{r}_{\text{TX}}|) dS', \quad (2.1)$$

where  $E_z^i$  is the incident field in the direction of  $\hat{z}$ ,  $k_0$  is the wavenumber in free space,  $I_e$  is the constant current amplitude in the infinite line source,  $\epsilon_0$  is the permittivity in free space,

$H_0^{(2)}$  is the Hankel function of the second kind of order zero,  $\mathbf{r}$  is the receiver location on the  $xy$ -plane, and  $\mathbf{r}_{\text{TX}}$  is the location of the transmitter (the line source).

From Equation 2.1, we can see that the electric line source is indeed constant over  $z$ :  $E_z^i$  is a function of  $\mathbf{r}$  but not  $z$ . Moreover, the incident field on  $\hat{z}$  is the total incident field, i.e.  $E_z^i = E^i$ , because the incident field's radial and angular components on the  $xy$ -plane are both zero [32].

With the duality theorem, one can deduce the field generated by a magnetic line source from the solution of an electric line source. Similarly, there will be a magnetic field  $H_z^i$  that is constant along  $\hat{z}$ . However, magnetic sources have not been known to be physically realizable; they can be used as equivalent sources for aperture antennas [33]. So we will stick with the electric line source and use the electric field for forthcoming mathematical representations and narratives.

In free space, the incident wave propagation in Equation 2.1 is the total field. What if any scatters are present? Then an additional component is introduced to the total field: scattered field. By the superposition, the total field is a summation of the incident field and the scattered field,

$$E(\mathbf{r}) = E^i(\mathbf{r}) + E^s(\mathbf{r}). \quad (2.2)$$

With the volume equivalence principle, the derivation of the exact scattered field in the form of an integral equation from Maxwell's equations is listed in Appendix A. More explicitly, with an

electric line source, the scattering phenomenon is governed by the electric field integral equation (EFIE) as Equation A.14,

$$\begin{aligned} E(\mathbf{r}) &= E^i(\mathbf{r}) + E^s(\mathbf{r}) \\ &= E^i(\mathbf{r}) - \frac{jk_0^2}{4} \int_S (\epsilon(\mathbf{r}') - 1) E(\mathbf{r}') H_0^{(2)}(k_0 |\mathbf{r} - \mathbf{r}'|) dS', \end{aligned} \quad (2.3)$$

where  $E$ ,  $E^i$ , and  $E^s$  are the total, the incident, and the scattered fields,  $k_0$  is the wave number in free space,  $\epsilon$  is the complex relative permittivity, and  $S$  is the investigation domain. The complex relative permittivity is a dimensionless number,

$$\epsilon = \epsilon' - j \frac{\sigma}{\omega \epsilon_0}, \quad (2.4)$$

which consists of the real dielectric permittivity  $\epsilon'$  and the imaginary part that is due to the conductivity  $\sigma$ . We assume a free space permeability throughout this work.

The EFIE, i.e. Equation 2.3, describes electromagnetic scattering. This very equation is the mathematical representation for the forward and the inverse scattering both; the only difference is which variables are known and which are not.

### 2.1.2 Scattering Problem

Electromagnetic scattering is a classic topic among many in electromagnetics [34, 35]. It asks for electromagnetic fields reflected by a scatterer with known properties, such as its shape, landscape, permittivity, and permeability.

Here, with a full knowledge of permittivity  $\epsilon(\mathbf{r}')$ , the forward scattering problem solves for the electric field  $E(\mathbf{r})$ . Depending on the location of the unknown electric field, the forward scattering problem can be broken into two cases,

$$E(\mathbf{r}) - E^i(\mathbf{r}) = -\frac{jk_0^2}{4} \int_S (\epsilon(\mathbf{r}') - 1) E(\mathbf{r}) \mathbf{H}_0^{(2)}(k_0|\mathbf{r} - \mathbf{r}'|) dS', \quad \mathbf{r} \in S, \quad (2.5a)$$

$$E(\mathbf{r}) - E^i(\mathbf{r}) = -\frac{jk_0^2}{4} \int_S (\epsilon(\mathbf{r}') - 1) E(\mathbf{r}) \mathbf{H}_0^{(2)}(k_0|\mathbf{r} - \mathbf{r}'|) dS', \quad \mathbf{r} \notin S. \quad (2.5b)$$

These two equations look similar but  $E(\mathbf{r})$  in both equations are quite different because of the domain of  $\mathbf{r}$ . Equation 2.5a calculates the internal field inside the scatterer ( $\mathbf{r} \in S$ ), while Equation 2.5b calculates the electric field outside the scatterer ( $\mathbf{r} \notin S$ ).

In Equation 2.5a, with  $\mathbf{r} \in S$ , the unknown internal field inside the scatterer appears both outside and inside the integrand; this is a Fredholm equation of the second kind in Appendix A.4. After solving Equation 2.5a for the internal field, one can plug that information into the integrand of Equation 2.5b and solve for the total field outside the scatterer,  $E(\mathbf{r})$ ,  $\mathbf{r} \notin S$ .

### 2.1.3 Inverse Scattering Problem

For inverse scattering problems, the electromagnetic properties of targets are inquired by the knowledge of the scattered field. The sensing process starts from a known source transmitting the electric field, which illuminates the target under investigation; by observing corresponding scattered field outside the investigation domain, one aims to map the dielectric permittivity and the conductivity inside the investigation domain.

In contrast to forward scattering problems, the inverse ones solve for the relative permittivity distribution instead of the scattered field. In a two-dimensional inverse scattering problem with a tomographic configuration in Figure 1, there are

- known input: incident field in free space,  $E^i(\mathbf{r})$ ,  $\mathbf{r} \in S \cup \mathbf{r} \notin S$ ;
- observable output: total field outside the investigation domain,  $E(\mathbf{r})$ ,  $\mathbf{r} \notin S$ ;
- unknown system: permittivity of the investigation domain,  $\epsilon(\mathbf{r}')$ ,  $\mathbf{r}' \in S$ .

Therefore, to represent inverse problems, one confines  $\mathbf{r} \notin S$  in the EFIE Equation 2.3,

$$E(\mathbf{r}) = E^i(\mathbf{r}) - \frac{jk_0^2}{4} \int_S (\epsilon(\mathbf{r}') - 1) E(\mathbf{r}') H_0^{(2)}(k_0 |\mathbf{r} - \mathbf{r}'|) dS', \mathbf{r} \notin S. \quad (2.6)$$

The unknown  $\epsilon(\mathbf{r}')$  only appears within the integrand. If we also know the internal field  $E(\mathbf{r}')$ , Equation 2.6 would be a Fredholm integral equation of the first kind as deconvolution with the kernel function is the Hankel function.

However, within the integrand of Equation 2.6, the internal fields in the scatterer  $E(\mathbf{r}')$  is also a function of the unknown permittivity  $\epsilon(\mathbf{r}')$ , where the forward scattering Equation 2.5a kicks in. The inverse and the forward problems intertwine as solving Fredholm integral equations of the first kind requiring the second: Fredholm integral equations of both kinds emerge subsequently throughout the electromagnetic inverse scattering problems. This determines the nonlinearity in inverse scattering problems.

## 2.2 Previous Solutions

Despite of the relative simplicity of the sensing phenomenon, inverse electromagnetic scattering problems are characterized by challenging mathematical difficulties such as non-linearity and ill-posedness [36,37]. Many researchers have approached this nonlinear and ill-posed inverse problem and attempts have been made from several perspectives.

1. Continuous to discrete: Liouville-Neumann infinite series are used to solve Fredholm integral equations. The continuous electric field integral equation can be numerically implemented with finite series, such as the Method of Moment [38] and the Finite Element Method [39]. Discretization usually involves a summation of series, and with the discrete equation, one can numerically calculate the solution with matrices.

2. Non-linear to linear: linearity can be approximated by the first-ordered Born/Rytov approximation, but this sacrifices the exact electromagnetic model [40]. If we use the Born/Rytov approximation to turn the EFIE of inverse problems into linear first-kind Fredholm integral equation; once solving the first kind integral equation for permittivity, one plugs that recent permittivity distribution in the forward scattering of the second kind Fredholm integral equation and calculates the inner fields. These two kinds of equations take turns during an iterative search for the permittivity solution.

3. Deterministic to stochastic: for an ill-posed inverse problem, regularization schemes are often applied to achieve a stable solution [36]. Stochastic global optimizations consume more computational loads but provide a different perspective. However, there is no free lunch [41] for stochastic algorithms in machine learning.

4. Space domain to other domains: instead of directly solving the permittivity at each pixel, the unknown vector is projected to the Fourier domain or the wavelet domain to reduce the number of unknowns. Reconstructable Fourier harmonics of the unknown permittivity are applied with linear and quadratic approaches [42]. Wavelet-based reconstruction has been widely in sensing, such as the total-variation compressive sensing [43] and oil detection.

5. Isotropic to dyadic contrast function: most inverse scattering approaches consider the use of an isotropic contrast function, which is mathematically represented with a complex valued function of the position. An improvement was presented in [44], where a dyadic contrast function was introduced to account for depolarization effects in the case of an incident field that illuminates structures consisting of thin cylinders.

In the following sections, we will talk about some of these solutions with more details.

### 2.2.1 Approximations

With proper assumption upon the unknown scatterer, we can apply approximations to the electric field inside the scatterer. Some of these approximations can linearize the nonlinear inverse problem.

The first-order Born approximation [45, 46] substitutes the unknown fields in the scatterer with the free space incident fields. Therefore it describes weak scatterer better [47]. Linearizing the nonlinear inverse scattering problem, the Born approximation starts initial iteration for the iterative Newton's method. The second-order Born approximation substitutes the unknown fields in the scatterer with calculated fields in the scatterer by the first-order Born approximation. This quadratic equation does not linearize our problem, yet provides better reconstructions

than the linear Born model [48]. A high-order generalized extended Born approximation can efficiently approximate electromagnetic scattering problems [49].

The Rytov approximation is a first-order approximation for the complex phase of the field in the scatterer [50]; it neglects the phase variation of the scattered field inside of the scatterer. And this approximation can also make the electric field integral equation linear.

The Kirchhoff approximation is for perfectly electric conductor (PEC) scatterers. By means of the Kirchhoff approximation, nonlinear unknown to data mapping is then linearized and reduced it into a Fourier transform [51]. At a large wavelength, the scattered field is approximated at a point, where the the boundary is replaced by its tangent, as recalled in the Huygens' principle.

### **2.2.2 From Nonlinear to Linear: Born Related Methods**

The inverse problem can be described as Fredholm integral equation of the first kind, if the internal field  $E(\mathbf{r}')$  is known. However, the unknown parameter,  $\epsilon(\mathbf{r}')$ , is needed to calculate the electric fields within the object,  $E(\mathbf{r}')$ . Therefore, both of them become unknown and the EFIE is nonlinear.

To tackle its nonlinear property, one can approximate inverse scattering problems with the Born approximation, which assumes that the total field in the scatterer  $E(\mathbf{r}')$  is approximated with the incident field as

$$E(\mathbf{r}) = E^i(\mathbf{r}) - \frac{jk_0^2}{4} \int_S (\epsilon(\mathbf{r}') - 1) E^i(\mathbf{r}') H_0^{(2)}(k_0|\mathbf{r} - \mathbf{r}'|) dS', \mathbf{r} \notin S, \quad (2.7)$$

where the incident field  $E^i(\mathbf{r}')$  replaces the total field  $E(\mathbf{r}')$  in Equation 2.6. Now every component in the integrand is known except the unknown  $\epsilon(\mathbf{r}')$  so the inverse problem of Equation 2.7 is linear.

For a weak scatterer that has a low permittivity contrast to free space, its internal field could be close to the field in free space as the Born approximation stands, so efficient reconstruction results could be obtained. However, when strong scatterers are present, the Born approximation is no longer valid. Fortunately, for strong scatterers, we can still apply the results from the Born approximation to develop iterative methods like the Newton's methods. In general, with the Born approximation, one can solve the linear Equation 2.7 for permittivity; this permittivity result would update the field information, which in turns would update previous permittivity results; the permittivity and internal field will be iteratively updated until they converge. The following text is to describe these iterative procedures.

There are two major iterative methods developed to iteratively approach  $\epsilon(\mathbf{r}')$  based on the Born approximation, the Born iterative method (BIM) [52] and the distorted Born iterative method (DBIM) [53]. For both iterative methods, the Born approximation is assumed to start the initial step: the unknown internal field  $E(\mathbf{r}')$  is approximated with the fields in free space  $E^i(\mathbf{r}')$  similar to Equation 2.7 as

$$E(\mathbf{r}) = E^i(\mathbf{r}) - \frac{jk_0^2}{4} \int_S (\epsilon^{(0)}(\mathbf{r}') - 1) E^i(\mathbf{r}') H_0^{(2)}(k_0|\mathbf{r} - \mathbf{r}'|) dS', \mathbf{r} \notin S. \quad (2.8)$$

Once solving the forward scattering problem Equation 2.8 to obtain permittivity distribution  $\epsilon^{(0)}(\mathbf{r}')$  as the initial step, one updates the internal field within the scatterer as  $E^{(1)}(\mathbf{r}')$  by enforcing  $\mathbf{r} \in S$ . Generally, at  $n$ -th iteration, BIM solves  $E^{(n)}(\mathbf{r}')$  with

$$E^{(n)}(\mathbf{r}) = E^i(\mathbf{r}) - k_0^2 \int_S (\epsilon^{(n-1)}(\mathbf{r}') - 1) E^{(n)}(\mathbf{r}') H_0^{(2)}(k_0 |\mathbf{r} - \mathbf{r}'|) dS', \mathbf{r} \in S \quad (2.9)$$

and insert solved  $E^{(n)}(\mathbf{r}')$  into the inverse problem for  $\epsilon^{(n)}(\mathbf{r}')$ ,

$$E(\mathbf{r}) = E^i(\mathbf{r}) - \frac{jk_0^2}{4} \int_S (\epsilon^{(n)}(\mathbf{r}') - 1) E^{(n)}(\mathbf{r}') H_0^{(2)}(k_0 |\mathbf{r} - \mathbf{r}'|) dS', \mathbf{r} \notin S. \quad (2.10)$$

Repeat these procedures until the solution of  $\epsilon^{(n)}(\mathbf{r}')$  converges or the termination criterion is met.

In BIM, by assumption, the kernel Green's function remains the homogeneous free space Green's function shown as the Hankel function of the second kind of order zero. While in DBIM, besides all the procedures following BIM, the kernel Green's function  $G^{(n)}(|\mathbf{r} - \mathbf{r}'|)$  is inhomogeneous and updated with respect to solved  $\epsilon^{(n-1)}(\mathbf{r}')$  at each iteration. Due to these updated Green's functions DBIM converges faster, while BIM appears to be more robust to noise. The DBIM has been proved as equivalent to the Newton-Kantorovich's method [54], and the Newton-Kantorovich algorithm has been applied to shape detection for PEC [55]. Both BIM and DBIM were developed for dielectric permittivity and not for highly conductive objects, because the Method of Moment assumes a constant electric field in a pixel, which is not representative for conductive surfaces.

Overall, with the Born approximation, the nonlinear inverse scattering integral equation becomes a linear functional equation. This very functional equation can be numerically calculated using the Finite Element Method, the Method of Moment (MoM), etc. Thus this linear inverse problem can be represented as an algebraic system of linear equations, hence it can be accelerated by parallel computing [56]. We will review the discretization of the functional with MoM next.

### 2.2.3 Method of Moment - Discretization of EFIE

To numerically calculate fields and permittivity, one needs to discretize the EFIEs into matrix forms and then solve a system of linear algebraic equations. For the tomographic configuration shown in Figure 2a, we discretize the domain  $S$  into  $N$  pixels, and assume homogeneous permittivity and internal field distribution at  $n$ -th pixel  $S_n$  as illustrated in Figure 2b.

Around the investigation domain  $S$ , let there be  $N_{\text{TX}}$  transmitters and  $N_{\text{RX}}$  receivers, which lead to  $N_{\text{TX}}N_{\text{RX}}$  observations of the scattered field. And we consider the TM-mode line source as the transmitter for this 2D problem. For the  $m$ -th transmitter-receiver combination, the total field  $E$  observed at the corresponding receiver is

$$E_m = E_m^i - \frac{jk_0^2}{4} \sum_{n=1}^N (\epsilon_n - 1) E_n \int_{S_n} \text{H}_0^{(2)}(k_0 |\mathbf{r}_m - \mathbf{r}'_n|) dS', \quad \mathbf{r}_m \notin S, \quad (2.11)$$

where  $\epsilon_n$  is the relative permittivity within the  $n$ -th pixel,  $\mathbf{r}_m$  is the location of  $m$ -th TX/RX combination, and  $\mathbf{r}'_n$  is the center of the  $n$ -th pixel.

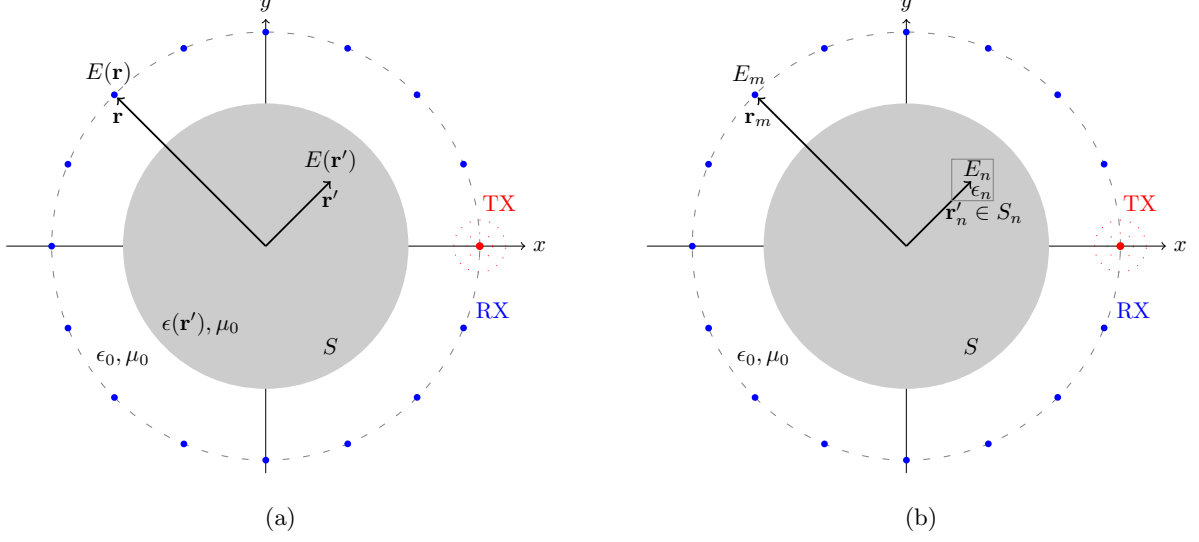


Figure 2: The tomographic configuration for inferring permittivity in: (a) a continuous form; (b) a discrete form.

Whereas Equation 2.11 relates the scattered field data outside the scatterer ( $E_m^s = E_m - E_m^i$ ,  $\mathbf{r}_m \notin S$ ) with the pixel permittivity  $\epsilon_n$  for the inverse problem, we also need the relation between the internal field  $E_n$  in the  $n$ -th pixel and the permittivity  $\epsilon_n$  for the forward problem. By enforcing  $\mathbf{r} \in S$  while discretizing Equation 2.5a, the total field at the  $p$ -th pixel,  $E_p$ , is represented as

$$E_p = E_p^i - \frac{jk_0^2}{4} \sum_{n=1}^N (\epsilon_n - 1) E_n \int_{S_n} \mathbf{H}_0^{(2)}(k_0 |\mathbf{r}_p - \mathbf{r}'_n|) dS', \quad \mathbf{r}_p \in S, \quad (2.12)$$

where  $E_p^i$  is the incident field at  $p$ -th pixel. Equation 2.12 can be written in a matrix form so that one can solve for internal electric field at each pixel with given permittivity.

For both Equation 2.11 and Equation 2.12, the integral of zero-order Hankel function over the circular region  $S_n$  can be approximated,

$$-\frac{jk_0^2}{4} \int_{S_n} \text{H}_0^{(2)}(k_0|\mathbf{r}_p - \mathbf{r}'_n|) \text{d}S' = \begin{cases} -\frac{j\pi k_0 r_{\text{eq}}}{2} \text{H}_1^{(2)}(k_0 r_{\text{eq}}) - 1, & \text{if } p = n \\ -\frac{j\pi k_0 r_{\text{eq}}}{2} \text{J}_1(k_0 r_{\text{eq}}) \text{H}_0^{(2)}(k_0|\mathbf{r}_p - \mathbf{r}'_n|), & \text{otherwise} \end{cases} \quad (2.13)$$

where  $r_{\text{eq}}$  is the equivalent radius of the discretized pixel,  $\text{H}_1^{(2)}$  is the Hankel function of the second kind of first order, and  $\text{J}_1$  is the Bessel function of the first kind.

With the discrete representation of the electric field and the permittivity in the inverse Equation 2.11 and the forward Equation 2.12, one can write these integral equations in a matrix form; the system of linear equations of inverse problem, Equation 2.11, can be seen as

$$\mathbf{d}_{(N_{\text{TX}}N_{\text{RX}},1)} = \mathbf{L}_{(N_{\text{TX}}N_{\text{RX}},N)} \mathbf{X}_{(N,1)}. \quad (2.14)$$

Here the scattered field data,  $\mathbf{d} \in \mathbb{C}$ , is the vector of the observable total field minus the incident field and its  $m$ -th element is

$$d_m = E_m - E_m^i, \quad (2.15)$$

where  $E_m$  is the total field and  $E_m^i$  is the incident field at the  $m$ -th TX/RX combination. The linear operator matrix,  $\mathbf{L} \in \mathbb{C}$ , in Equation 2.14 has its element

$$L_{m,n} = -\frac{jk_0^2}{4} E_n \int_{S_n} H_0^{(2)}(k_0 |\mathbf{r}_m - \mathbf{r}'_n|) dS', \quad (2.16)$$

where  $E_n$  is the electric field at  $n$ -th pixel, and the integral of the Hankel function can be numerically calculated as suggested in Equation 2.13. Finally, the unknown model parameter  $\chi$  is the relative permittivity contrast with the element

$$\chi_n = \epsilon_n - 1, \quad (2.17)$$

which is the relative permittivity contrast at  $n$ -th pixel.

With the matrix form shown as Equation 2.14, not only could we numerically compute the EFIEs, but also optimization can be formulated and solved as we will see in the next section.

#### **2.2.4 Optimization and Parameter Estimation**

The nonlinear inverse scattering problem can be linearized with the Born or the Rytov approximation and discretized with numerical methods, then it takes the matrix form of a dense system of linear equations as Equation 2.14. The reconstructed permittivity is obtained in an iterative method or not, we need to solve the ill-conditioned linear equations [57] regardless. Also, the number of data  $\mathbf{d}$  is fewer than number of unknown permittivity; the system equations are underdetermined. For such an underdetermined system, there are infinite solutions.

Naturally, picking a good solution with optimization becomes crucial and this section reviews some common approaches.

#### 2.2.4.1 Deterministic Regularizations

Optimization problems can be in the form of discrete least-squared problems. Besides optimizing an  $\ell_2$  like Equation 2.18 or an  $\ell_1$  norm, a joint  $\ell_1 - \ell_2$  norm-based regularization was applied in BIM [58]. Also, the contrast source inversion method [59] uses a deterministic minimization.

Regularizations are widely applied in solving discrete least-squared problems. In the original BIM and DBIM, the classic Tikhonov regularization was used. The traditional zero-order Tikhonov regularization [60] picks the solution not only minimizing the residual but also controlling the solution as

$$\min(\|\mathbf{d} - \mathbf{L}\boldsymbol{\chi}\|_2 + \gamma\|\mathbf{I}\boldsymbol{\chi}\|_2), \quad (2.18)$$

where  $\gamma$  is the regularization parameter compromising between the residual and the solution, and  $I$  is the identity matrix. Even if no general procedures can determine the optimal  $\gamma$ , it is possible to tune the regularization parameter based on the reconstruction results. Therefore, the subjectivity of the Tikhonov regularization is introduced.

There are two categories, direct and iterative regularization methods. Direct regularization methods include the Tikhonov regularization, Singular Value Decomposition (SVD) [61], and Truncated Singular Value Decomposition (TSVD). Iterative regularization methods include Conjugate Gradient (CG) [62], complex conjugate gradient methods, and Algebraic Reconstruction Technique (ART). When the operator  $\mathbf{L}$  is a large matrix and dense, regularizations

solved by iterative methods can be handy since they do not store large matrices (no need of huge memory as direct methods do), even though their convergence rate cannot be always guaranteed with theoretical results [63].

#### **2.2.4.2 Stochastic Evolutionary Optimization Algorithms**

The difference between the calculated electric field with predicted permittivity and the observed electric field naturally forms the loss function of a global optimization problem, which allows researchers to tackle the traditional nonlinear inverse problem from an optimization perspective without approximations. Consequently, the goal becomes to minimize the residual, which are also called the fitness function or the cost function.

Among many optimization approaches, algorithms in natural computing are inspired from nature [64]. During the last two decades, such a family of algorithms for global optimization inspired by biological evolution have emerged; basically, they are a population-based trial and error by introducing randomness and stochastically eliminating less favorable solutions. Stochastic approaches [17], such as genetic algorithms, particle swarm optimizations, and ant colony optimizations, have been applied to crack such a minimization problem.

Genetic algorithms are commonly applied in electromagnetics [65], antenna design [66], [67], and crack identification for nondestructive testing [68]. It is an iterative algorithm mimicking the biological mechanism in evolution. The set of trial solution, called the population, evolves over successive generations based on procedures such as selections, crossover, and mutation until the population converges. The algorithm starts from an initial population of proposed

solutions; these solutions can be randomly generated or based on some priori knowledge of the solution.

In electromagnetic scattering problems, the priori knowledge about permittivity is that the real part of the relative permittivity is larger than one and the imaginary part is less than zero. More specifically, the prior knowledge can be obtained from the earlier reconstruction results. Once the fitness function of each element in the initial population is evaluated, the elements that offer less residual would be selected: this is the selection procedure. This selection provides candidates for crossover and mutation procedures for the next generation. The crossover procedure generated a new population by combining these selected elements. Then the mutation adds some randomness to this new population as the new generation. The new generation will be through the same procedures of selection, crossover, and mutation until the stopping criterion is met.

More evolutionary algorithms include memetic algorithms [69] and the Ant Colony Optimization (ACO) as a part of Swarm Intelligence [70], which has been compared with stochastic Gradient Descent [71]. Researchers have also combined natural computing algorithm: hybrid of particle swarm optimization for distribution state estimation [72] and hybrid of evolutionary and particle swarms [73].

Besides the hybrid between nature-inspired stochastic methods, another type of hybrid is to combine the regularization in direct solving nonlinear equations and the metaheuristic in global optimization to benefit from specific features of each. For example, the classic Born iterative approaches with regularization converge to solutions faster; the population-based al-

gorithms might avoid solutions trapped in local minima. In [74], nonlinear problem is directly solved with GA, which was cascaded with the conjugate gradient method to map homogeneous cylinders; they explore the global solution first then seek for fast convergence from CG. The residual is minimized by genetic algorithms and compared with first and second order Born approximations. Inspired by this hybrid idea, we will share our efforts into combinations of BIM and stochastic methods in Chapter 3.

### 2.3 Roadmap

The road map for this work is shown as Figure 3. This chapter reviews necessary theoretical background in blue for Chapter 3 and Chapter 4. Chapter 3 contains the work in green on the top and right. Chapter 4 contains work in green at the bottom.

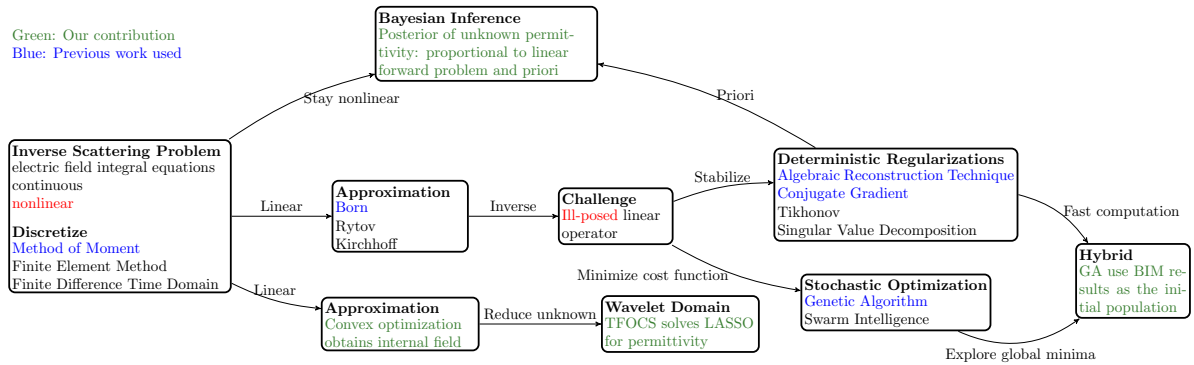


Figure 3: Roadmap

## CHAPTER 3

### STOCHASTIC METHODS AND BAYESIAN INFERENCE

*Part of this chapter was published in conference proceedings, 2020 43rd International Conference on Telecommunications and Signal Processing (TSP) [1] and 2021 XXXIVth General Assembly and Scientific Symposium of the International Union of Radio Science (URSI GASS) [2]. Copyright © 2020, IEEE. Copyright © 2021, IEEE.*

“The actual science of logic is conversant at present only with things either certain, impossible, or entirely doubtful, none of which (fortunately) we have to reason on. Therefore the true logic for this world is the calculus of Probabilities, which takes account of the magnitude of the probability which is, or ought to be, in a reasonable man’s mind.”

---

James Clerk Maxwell

This chapter presents results of stochastic methods applied in inverse scattering. We use the BIM results and feed them into: 1. genetic algorithms (GA) as the initial population; 2. Monte Carlo Markov Chain as priori knowledge for Bayesian inference. Statistical inversions using Bayesian approaches can produce various estimates over a probability distribution and further evaluate their credibility [75]. Moreover, the Bayesian approach exploits our prior beliefs in the

unknown and copes with randomness such as noise or uncertainty brought by discretizations in a systematic way.

### 3.1 A Hybrid of BIM and GA

In Equation 2.14, the electric field data  $\mathbf{d}$  are related to the permittivity contrast  $\boldsymbol{\chi}$  via the operator  $\mathbf{L}$ . To estimate the model parameter  $\boldsymbol{\chi}$ , we are trying to find a set of parameters that minimize the difference between the measurements and the predictions from the forward scattering problem, i.e. the residual. The residual can be evaluated by finding the Euclidean norm,

$$\|\mathbf{d} - \mathbf{L}\boldsymbol{\chi}\|_2 = \sqrt{\sum_{m=1}^{N_{\text{TX}}N_{\text{RX}}} (d_m - (\mathbf{L}\boldsymbol{\chi})_m)^2}, \quad (3.1)$$

and the optimized solution minimizing this  $\ell_2$ -norm is a least square's solution. Recall that  $N_{\text{TX}}N_{\text{RX}}$  is the number of data points.

In linearized inverse problems, the apparent task is to solve for  $\boldsymbol{\chi}$ , but the solution is not unique due to the underdetermined system, which results from overnumbered measurements by discretization of the scatterer. Also, any small disturbance in  $\mathbf{d}$  might result in huge variations of the estimated solution  $\boldsymbol{\chi}$ , due to the ill-conditioned property of the linear operator  $\mathbf{L}$ .

There are two options to deal with this ill-conditioned property. First, if proper techniques to stabilize the inversions, called regularizations to find the solution, are needed, biased constraints would be introduced. Second, to explore the global search space, population-based stochastic optimization approaches would add randomness to proposed trial solutions. The inherent difference lies between the deterministic and the stochastic methods is whether the

solution completely relies on the initial condition and the approach parameters. Consequently, deterministic regularizations are mostly much faster than stochastic optimizations.

Moreover, in stochastic optimization approaches, the goal is to minimize the residual, which are also called the fitness function or the cost function and we can embed some priori knowledge in the stochastic approaches. For example, in electromagnetic scattering problems, the real part of the relative permittivity is larger than one, and the imaginary part is less than zero.

To combine the advantages of both regularizations and stochastic approaches, we apply a hybrid technique of existing methods to two-dimensional nonlinear inverse scattering problem, iterative regularizations and GA. Also, we exploit the advantages of setting up boundaries for the unknown permittivity. Overall, we apply regularizations to BIM for fast reconstruction results first, which then become good prior knowledge to feed into GA. In GA, boundaries for the solution were set up for homogeneous area as two standard deviation within the mean value of the deterministic results.

The first step of our method is the classic BIM. Due to the ill-conditioning of the linear matrix  $\mathbf{L}$ , regularization techniques are widely applied to stabilize the inversions. To minimize Equation 3.1, we use iterative regularization techniques, ART and CG. ART approaches the solution by sweeping the  $i$ -th the rows of  $\mathbf{L}$  at the  $j + 1$ -th iteration as

$$\boldsymbol{\chi}^{j+1} = \boldsymbol{\chi}^j + \lambda_j \frac{d_i - \langle \mathbf{L}_i, \boldsymbol{\chi}^j \rangle}{\|\mathbf{L}_i\|^2} \mathbf{L}_i^T, \quad (3.2)$$

where  $\boldsymbol{\chi}^j$  is the solution at the  $j$ -th iteration,  $\lambda_j$  is a tuning parameter controlling the speed of convergence,  $i = j \bmod M + 1$ . CG is known for solving linear equations with a positive-definite matrix; therefore, we apply it to solve  $\mathbf{L}^T \mathbf{L} \boldsymbol{\chi} = \mathbf{L}^T \mathbf{d}$ .

The second step is that the solution space is investigated by the means of a global optimization method. The population-based stochastic GA would add randomness to the regularization results as proposed trial solutions. The set of trial solutions, called the population, evolves over successive generations based on procedures such as selections, crossover, and mutation until the population converges. In GA, upper and lower bounds for a homogeneous area were set up as two standard deviation within the mean value of the deterministic results. In this way, the information resulting from the BIM method is exploited.

### **3.1.1 Numerical Results**

In this section, we present numerical results using BIM with 1) deterministic regularizations, ART and CG; 2) the proposed hybrid approach, where the BIM inversions are followed by the application of the GA algorithm. The solver for scattered fields and total fields is obtained by the Method of Moment [76] developed in MATLAB. Case studies include a homogeneous circular cylinder with  $\epsilon = 1.6$  and an inhomogeneous circular layered cylinder with outer  $\epsilon = 4$  and inner  $\epsilon = 2$ .

Scatterers are illuminated by TM-mode line sources at 1 GHz. There are 8 transmitters and 32 receivers located on the circumference of 1.5 times of the radius of the scatterer. Therefore, a multiview/multistatic configuration at single frequency is considered. The investigation domain

in the forward model is discretized into  $144 \times 144$  pixels, whereas  $36 \times 36$  pixels are considered for the inverse problem.

We initialize the BIM by assuming the permittivity equal to the one of the free space at the first iteration, and apply ART and CG to BIM until the solution converges. In our cases, BIM converges within 20 iterations. The deterministic methods used in this step cost less than 1 s.

Next, we use the BIM solution as the starting point of the GA approach; the mean and the standard deviation of the BIM retrieved permittivity are calculated so that the bounds for GA populations are twice of the standard deviation. At each generation of GA, the population size is 100, the elite count is 5, and the crossover fraction is 0.8. The cost function that GA is minimizing is the relative error with respect to a  $\ell_2$  norm between the scattered field data vector and the computed scattered field based on the proposed solution. For the homogeneous scatterer, GA terminates within 100 generations in 328 s with the error 0.24%. For the inhomogeneous case, the boundary between the two homogeneous areas is estimated by the maximum derivative of BIM results, and GA terminates at 200 generations in 795 s with the error of 2.36%.

In order to evaluate reconstructed permittivity, we use the root-mean-square deviation  $\hat{\sigma}$  as,

$$\hat{\sigma} = \sqrt{\frac{1}{n} \sum (\hat{\epsilon} - \epsilon)^2}, \quad (3.3)$$

where  $n$  is the length of the discretized permittivity vector,  $\hat{\epsilon}$  is the estimated permittivity vector, and  $\epsilon$  is the true one. Here we have 2 cases, a homogeneous scatterer with little contrast

permittivity ( $\epsilon = 1.6$ ), and an inhomogeneous layered scatterer (outer layer  $\epsilon = 4$ , inner layer  $\epsilon = 2$ ). All reconstructed results for the homogeneous area are compared in Table I.

TABLE I: MEAN AND RMS DEVIATION FOR FOUR METHODS

<b>Object</b>	$\epsilon$		<b>ART</b>	<b>CG</b>	<b>ART-GA</b>	<b>CG-GA</b>
Circular	1.6	mean	1.6004	1.6007	1.6011	1.6008
		$\hat{\sigma}$	0.0178	0.0248	0.0204	0.0284
Outer layer	4	mean	3.7111	3.4443	3.8592	3.5391
		$\hat{\sigma}$	0.277	0.2523	0.2917	0.2811
Inner layer	2	mean	2.2832	2.0502	2.159	1.8546
		$\hat{\sigma}$	0.4283	0.4491	0.4859	0.5179

### 3.1.1.1 A Homogeneous Scatterer: Permittivity of 1.6

The scatterer is a lossless homogeneous circular cylinder with relative permittivity  $\epsilon = 1.6$  and radius of  $0.5 \lambda$ . The reconstruction images are shown in Figure 4. To compare images, the reconstruction results along the horizontal slice are shown in Figure 5. Overall, BIM performs well for a relatively weak scatterer, where the Born approximation stands. ART offers

a smoother and more accurate reconstruction than CG. Based on the results of ART and CG, GA provides a more random reconstruction with a higher deviation.

### **3.1.1.2 A Layered Circular Cylinder**

In this inhomogeneous case, the cylinder of radius  $0.3 \lambda$  has the inner part with  $\epsilon = 2$  and radius  $0.225 \lambda$ , and its outer shell has  $\epsilon = 4$ . The reconstructed images using four methods are shown in Figure 6. All the reconstruction results along  $Y = 0$  are compared in Figure 7. ART outperforms not only the values but also identifying the edge, while CG seems lack of providing the homogeneous property of the inner layer. For GA, it is interesting to notice that, when hybrid with ART, it still shows the randomness and reconstructs relatively accurate range of values. However, when the hybrid with CG is applied, the reconstruction is not reliable, since it is not possible to achieve a quantitative reconstruction of the outer shell and also the reconstruction of the inner circle is not accurate.

### **3.1.2 Discussion**

A new hybrid combination of deterministic regularizations and stochastic GA are explored in BIM. The population-based genetic algorithm is meant to explore solutions that might not be trapped in local minima. The mean permittivity in the homogeneous area provided by GA are similar compared to the results from regularizations; however, GA also brings higher deviation due to its random nature. The limitation of GA is that information of trial solutions at each generation takes a single path to the final solution, and this path to solution is highly random. If the evolution of populations takes the “right” direction, the final results can be guaranteed; if the first a few generations evolves along a different direction, its offspring would be unlikely to

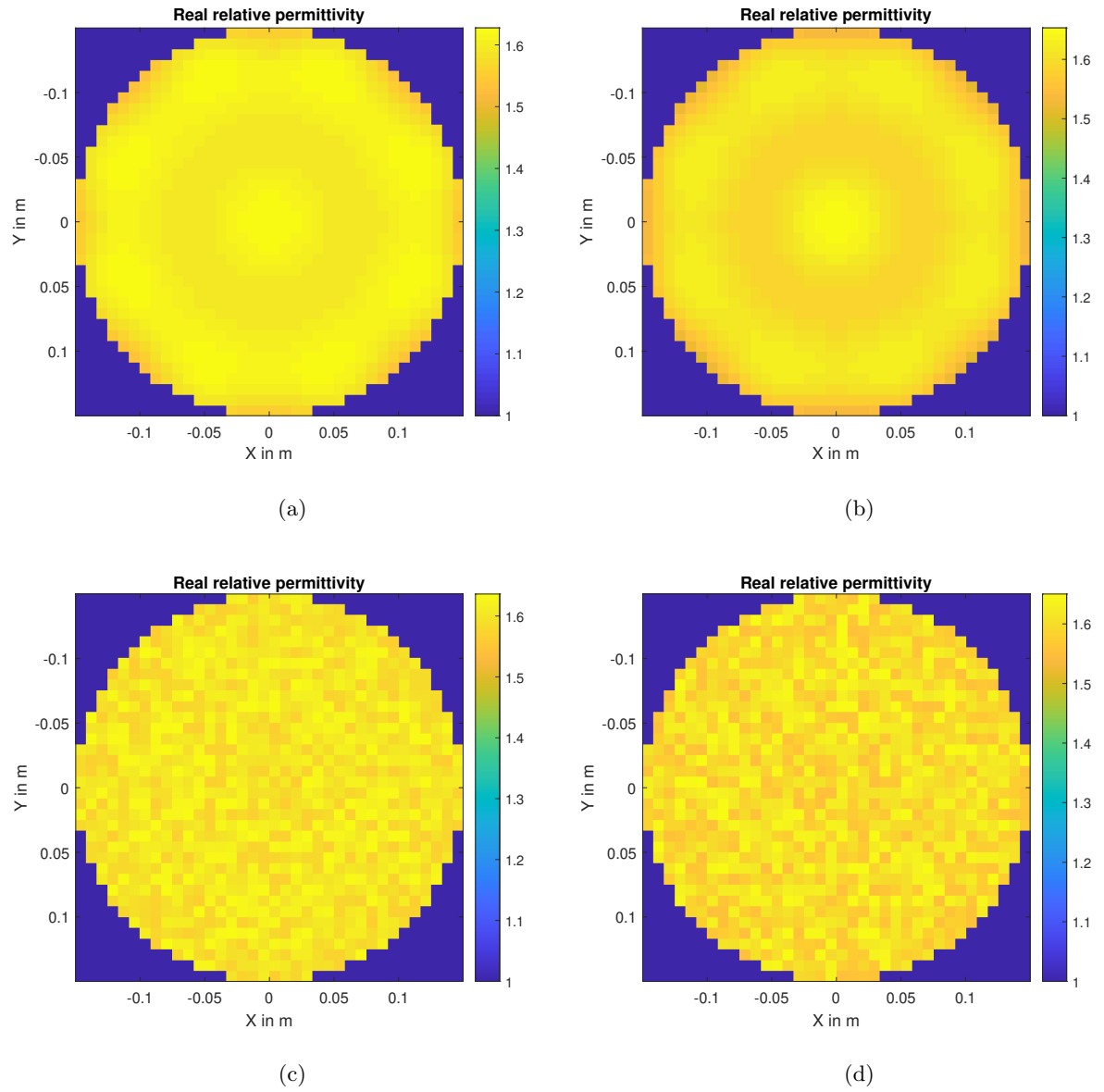


Figure 4: BIM reconstructed results for the permittivity within a cylinder,  $\epsilon = 1.6$ : (a) ART; (b) CG; (c) ART-GA hybrid; (d) CG-GA hybrid.

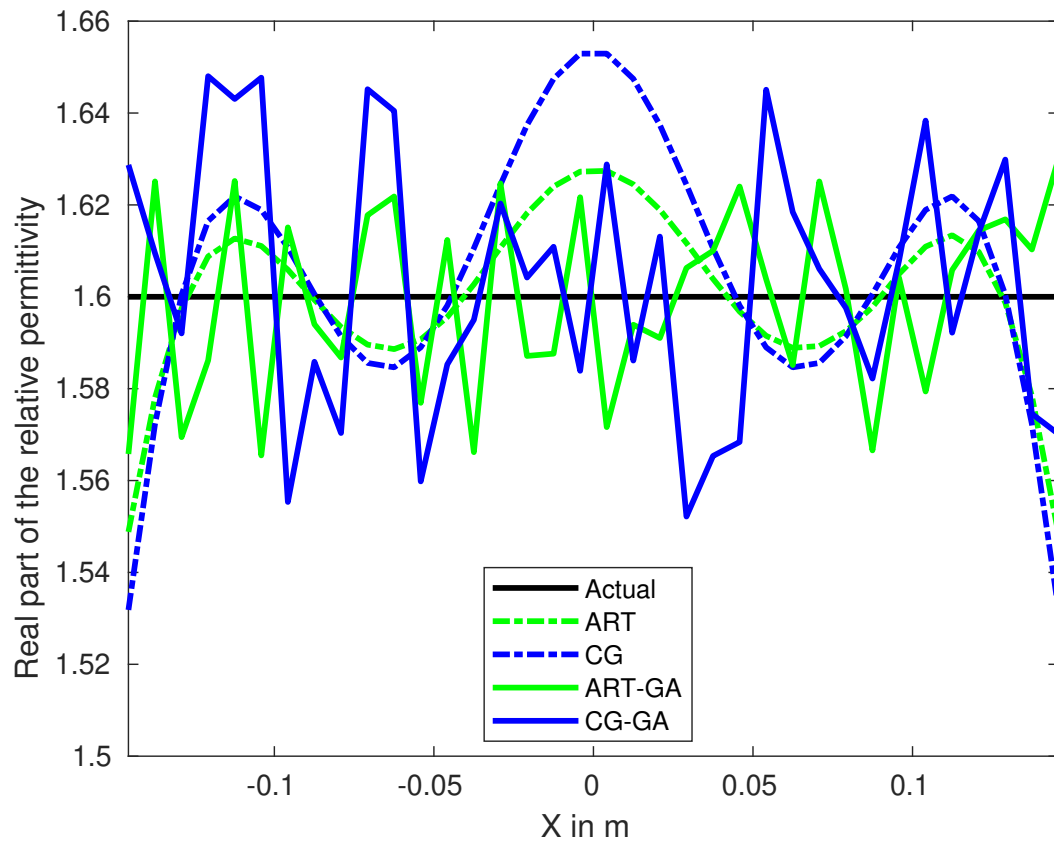


Figure 5: Cross sectional view of reconstructed relative permittivity along  $Y = 0$  for the homogeneous cylinder of  $\epsilon = 1.6$ .

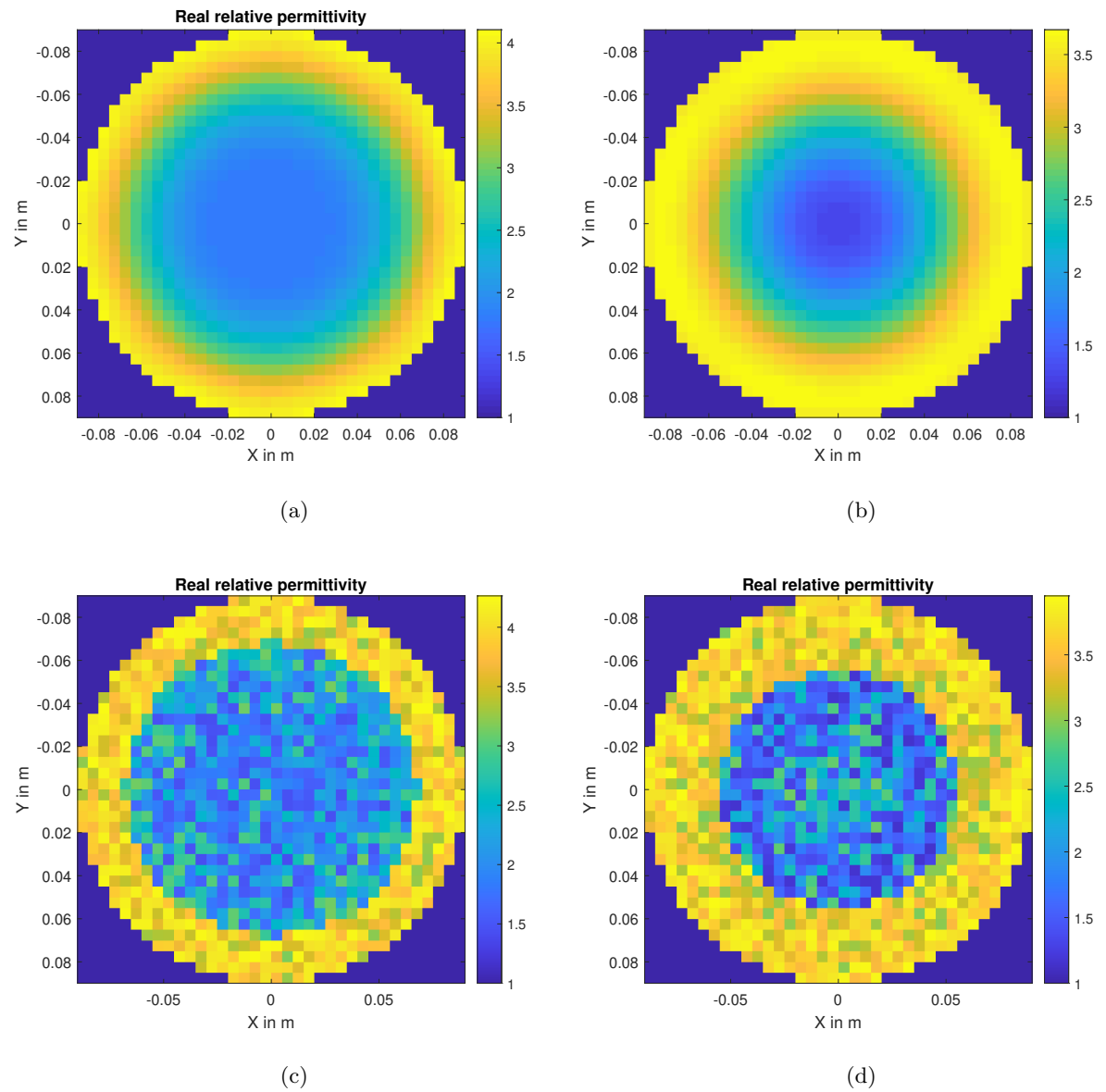


Figure 6: BIM reconstructed results for the permittivity within a layered cylinder, outer  $\epsilon = 4$ , inner  $\epsilon = 2$ : (a) ART; (b) CG; (c) ART-GA hybrid; (d) CG-GA hybrid.

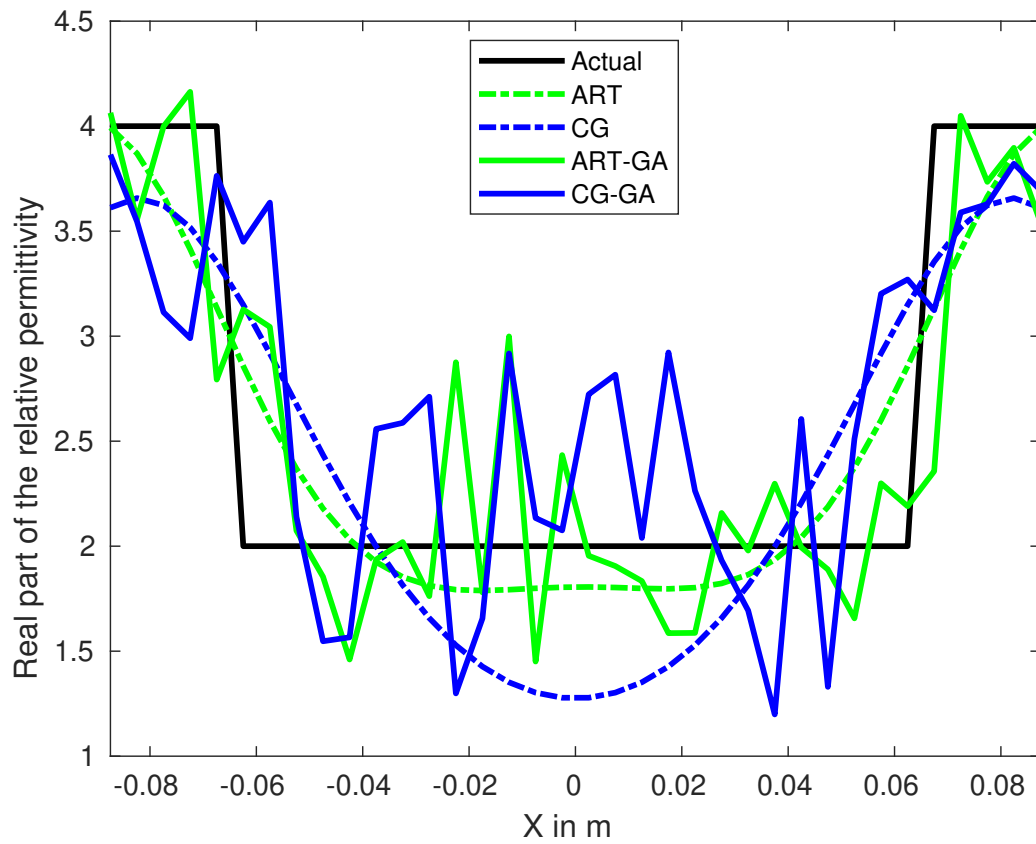


Figure 7: Cross sectional view of reconstructed relative permittivity along  $Y = 0$  for the layered cylinder with the outer layer of  $\epsilon = 4$  and the inner layer of  $\epsilon = 2$ .

take the “right” path back. Therefore this method is lack of the basic theorem of the Metropolis algorithm “(if you do this and this, then you generate samples of the distribution, in the precise, technical sense of sample)” [75]. We will introduce Bayesian inference with Metropolis algorithm next section.

### 3.2 Bayesian Inference

Remember that the least square problem might have multiple solutions and multiple minima due to the underdetermined ill-conditioned property of the linear operator. Instead of using regularizations to uncover the “best” fit for the unknown model parameters, now we consider measurements and parameters of a statistical model as random variables. Bayesian inference has been widely used in parameter estimation, for example, in electrical impedance tomography [77].

The Bayes theorem states that the distribution of unknown permittivity parameters  $\mathbf{X}$  conditioned on scattered field data  $\mathbf{D}$  is

$$P(\mathbf{X}|\mathbf{D}) = \frac{P(\mathbf{X})P(\mathbf{D}|\mathbf{X})}{P(\mathbf{D})}. \quad (3.4)$$

In Bayesian inverse models, the solution of an inverse problem takes the form of a posterior probability distribution,  $P(\mathbf{X}|\mathbf{D})$ , which is proportional to the prior multiplied by the likelihood. The likelihood of measured data  $\mathbf{D}$  given model parameters  $\mathbf{X}$ ,  $P(\mathbf{D}|\mathbf{X})$ , is strongly associated with the linear forward scattering model. The prior of  $\mathbf{X}$  depends on one’s prior information upon the unknown parameters. Particularly, the real part of the relative permittivity should be more than or equal to 1 and the conductivity should be positive. In addition,

reconstruction results from deterministic regularizations could be plausible priors; for example, previous reconstruction results from deterministic conjugate gradient regularizations offering upper and lower bounds. In that sense, Bayesian inference incorporates prior information to produce solutions for the model parameters.

On the one hand, to estimate the model parameters, one can choose the maximum a posteriori estimate (MAP), which maximizes the posterior density as

$$\mathbf{X}_{\text{MAP}} = \arg \max \pi(\mathbf{X}|\mathbf{D}). \quad (3.5)$$

Given the discrete forward scattering model  $\mathbf{d} = \mathbf{L}\boldsymbol{\chi} + \mathbf{N}$ , where  $\mathbf{N}$  is the noise vector with a Gaussian distribution to mimic the small variance in measured data and the prior is also Gaussian, one can find that the MAP solution is equivalent to the one by Tikhonov regularization. The MAP estimate provides a solution to an optimization problem.

On the other hand, the conditional mean (CM) of the unknown model parameter  $\mathbf{X}$  is another estimate

$$\mathbf{X}_{\text{CM}} = E\{\mathbf{X}|\mathbf{D}\} = \int_{\mathbb{R}^n} \mathbf{X}\pi(\mathbf{X}|\mathbf{D}) d\mathbf{X}, \quad (3.6)$$

where  $\pi(\mathbf{X}|\mathbf{D})$  is the posterior density. This conditional mean is the center of the posterior probability distribution. The CM estimate provides a solution to an integration problem, so usually it is more robust towards noise in the data than MAP. When the likelihood and the prior are both Gaussian, the posterior is also Gaussian and the MAP overlaps with CM.

Since the high dimension of the unknown discrete parameters requires a large sample space, it is challenging to numerically evaluate the integration for a conditional mean estimate. Here, the conditional mean is sampled in a statistical sense using the Monte Carlo Markov Chain (MCMC) methods, which can be applied favorably for our nonlinear inverse problem as they only depend on the linear forward model. The Monte Carlo integration draws samples from the posterior probability density and takes the average of these samples. Thus, we approximate the integral in Equation 3.6 with the population mean,

$$E\{\mathbf{X}|\mathbf{D}\} \approx \frac{1}{N} \sum_{t=1}^T \mathbf{X}_t \pi(\mathbf{X}_t|\mathbf{D}), \quad (3.7)$$

where the population mean is estimated by a sampled mean. Based on the laws of large number, the approximation becomes more accurate if  $T$  is increased, i.e. more samples are drawn from the distribution, when samples  $\mathbf{X}_t$  are independent. The question is how to sufficiently draw samples from the posterior distribution, especially in the case that drawing samples independently is not feasible. One option is to consider this distribution as the stationary distribution for a Markov chain.

A Markov chain is a sequence of random variables such that the next state only depends on the current state. In another words, the chain will gradually "forget" the initial state and eventually converges to the chain's stationary distribution. And this period of time for the chain to converge to its stationary distribution is called burn-in. So how to pick the stationary distribution for the chain as the posterior distribution we are trying to sample? To

construct a Markov chain, whose stationary distribution is our distribution of interest, we use the Metropolis-Hastings (MH) algorithm.

The MH algorithm is proved that the chain will eventually converges to its stationary distribution, and also the stationary distribution is the posterior distribution of interest. In other words, with the MH algorithm, a Markov chain converges to its stationary distribution, which is also the posterior distribution/inverse problem we are trying to sample. At each time  $t$ , one samples  $\mathbf{Y}$  from the proposal distribution. According to the acceptance ratio, the sample  $\mathbf{Y}$  is either accepted as the next state  $\mathbf{X}_{t+1}$  or not. In this work, we use the simplest MH algorithm, the random walk with a multivariate Gaussian proposal function, which has the proposal distribution,

$$q(\mathbf{Y}|\mathbf{X}) = q(|\mathbf{Y} - \mathbf{X}|). \quad (3.8)$$

This is a trial-and-error strategy; at each state  $t$ , we add some randomness to  $\mathbf{X}_t$  so that the proposed sample  $\mathbf{Y}$  explores the solution space: one samples  $Y$  from a proposal distribution, for example, a multivariate Gaussian distribution. According to the acceptance ratio, the sample  $Y$  is either accepted as the next state  $X_{t+1}$  or not. The algorithm flow is shown in Algorithm 1.

### **3.2.1 Numerical Results**

For a simple test case, we choose an infinitely long circular cylinder with the radius of  $\lambda/20$  and the relative permittivity of 11. This object with such a strong permittivity contrast is borrowed from [52]. A square that contains the circle with the side length of 0.03 m is the investigation domain. To avoid the inverse crime, the investigation domain,  $S$ , is divided into finer pixels ( $144 \times 144$ ) in the forward model than the inverse one ( $36 \times 36$ ). There are

---

**Algorithm 1** Metropolis-Hastings algorithm

---

**procedure** MH( $\mathbf{X}_0$ )  **for**  $t = 0 \dots T-1$  **do**    sample  $\mathbf{Y}$  from proposal distribution  $q(\cdot|\mathbf{X}_t)$     calculate acceptance ratio  $\alpha(\mathbf{X}_t, \mathbf{Y}) = \min(1, \frac{\pi(\mathbf{Y})q(\mathbf{X}_t|\mathbf{Y})}{\pi(\mathbf{X}_t)q(\mathbf{Y}|\mathbf{X}_t)})$     **if**  $Y$  is accepted, i.e. sample a random variable that is larger than  $\alpha(\mathbf{X}_t, \mathbf{Y})$  **then**       $\mathbf{X}_{t+1} = \mathbf{Y}$     **else**  $Y$  is rejected       $\mathbf{X}_{t+1} = \mathbf{X}_t$     **end if**  **end for****end procedure**

---

8 transmitters and 36 receivers that offer 288 measurements. TM-mode incident fields are radiated by a line source at 1 GHz and scattered fields are numerically calculated by MoM codes.

First, given the contour of the scatterer, we perform the traditional BIM with the conjugate gradient; Figure 8 shows the BIM results after 11 iterations: a rough range for the real part of the permittivity and quite accurate reconstructions of the conductivity.

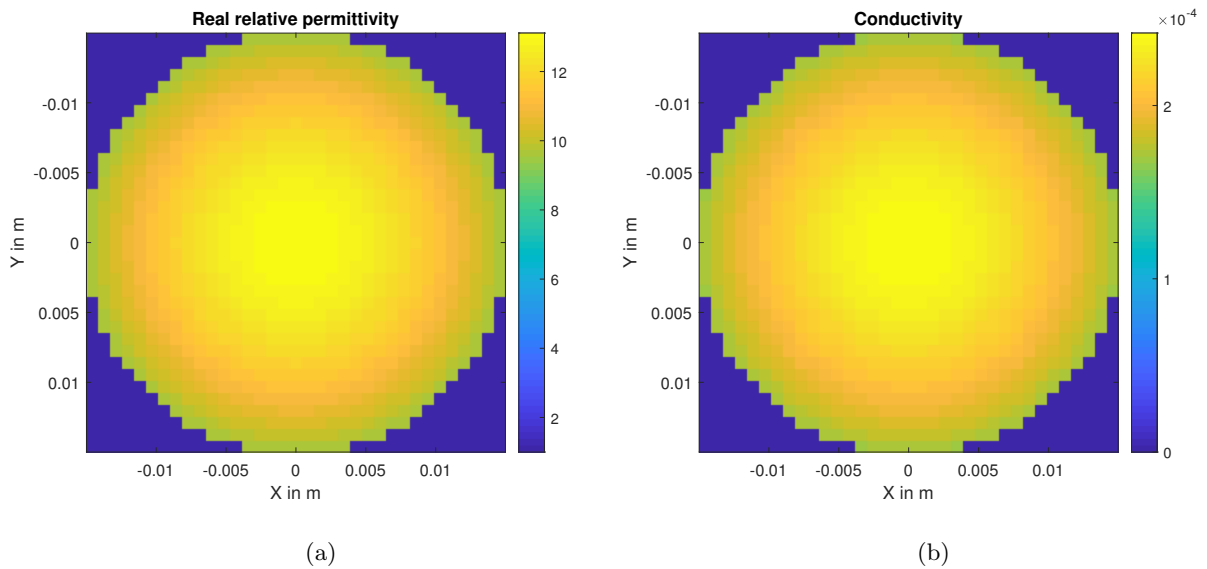


Figure 8: BIM reconstructed results for the permittivity within a cylinder,  $\epsilon = 11$ : (a) real part; (b) conductivity.

Then, for the real part of permittivity, we set the max/min values acquired in BIM as the upper/lower bounds for the permittivity random variable; for the imaginary part, we assume it is 0. The starting point of the Markov chain is the mean of the real permittivity at all pixels in the scatterer. As previous BIM results offer a good starting point, we don't throw away any iterations at the beginning of the chain; therefore no burn-in phase is needed. At each iteration, a random variable of the normal distribution with a standard deviation of 0.02 is added to the current state of permittivity values; this procedure generates a sample permittivity, which would be sent to the forward model to obtain the sample data. The difference between these sample data and scattered field data determines if this sample permittivity would be accepted as the next state of the chain. The longer the chain is, the closer the estimate is to the true posterior.

Figure 9 shows the reconstructed results of MCMC after 10000 iterations. The acceptance rate is 0.233. Due to the random nature of MCMC, the reconstructed permittivity profile in Figure 9(a) is not as smooth as the conjugate gradient results in Figure 8(a). However, even if the lower/upper bounds are set as  $[9.5, 13]$ , the conditional mean estimate by MCMC offers narrower bounds as  $[9.766, 12.815]$ . Moreover, the mean of the permittivity at all pixels by BIM is 11.180, which is improved by MCMC as 11.022; the standard deviation by BIM is 1.043, which is also improved by MCMC as 0.669. Figure 9(b) directly compares the permittivity reconstructions along 36 horizontal pixels at  $y = 0$  by BIM with the conjugate gradient and MCMC.

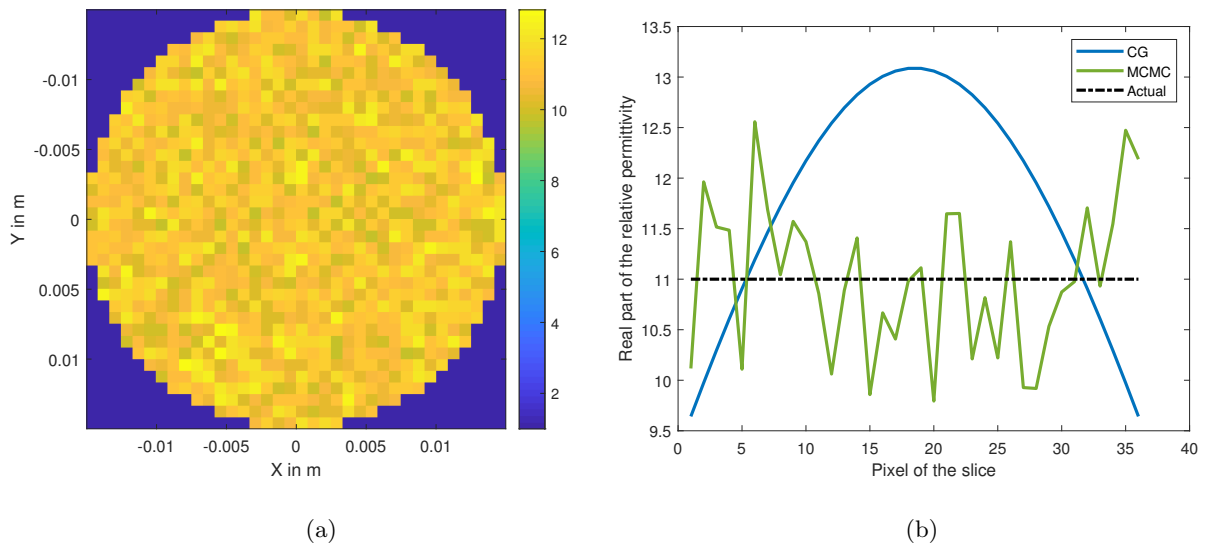


Figure 9: Reconstructed results for real part of the permittivity: (a) MCMC results within the cylinder; (b) slice comparisons along the horizontal axis.

Furthermore, we insert those reconstructed permittivity values into the forward model to compute scattered fields, which are compared with the analytical scattered field shown as in Figure 10. Not surprisingly, for forward model results, MCMC improves both of the amplitude and the phase of scattered fields. Since scattered fields are complex, we compare the amplitude by calculating the error as

$$\text{error} = \left| \frac{E_{\text{CG,MCMC}}^{\text{s}} - E_{\text{data}}^{\text{s}}}{E_{\text{data}}^{\text{s}}} \right|. \quad (3.9)$$

### 3.2.2 Discussion

Stochastic Bayesian inference is applied with priors from the BIM with the conjugate gradient technique. MCMC is computationally expensive compared to deterministic regularizations; however, MCMC does slightly improve the reconstructed permittivity profile for a scatterer with  $\epsilon = 11$ , where the Born approximation might fail. Like all previous methods mentioned, this method also needs some priori knowledge and outputs various solution with tuning parameters. In the next chapter, we will make efforts to reduce tuning parameters and priori knowledge.

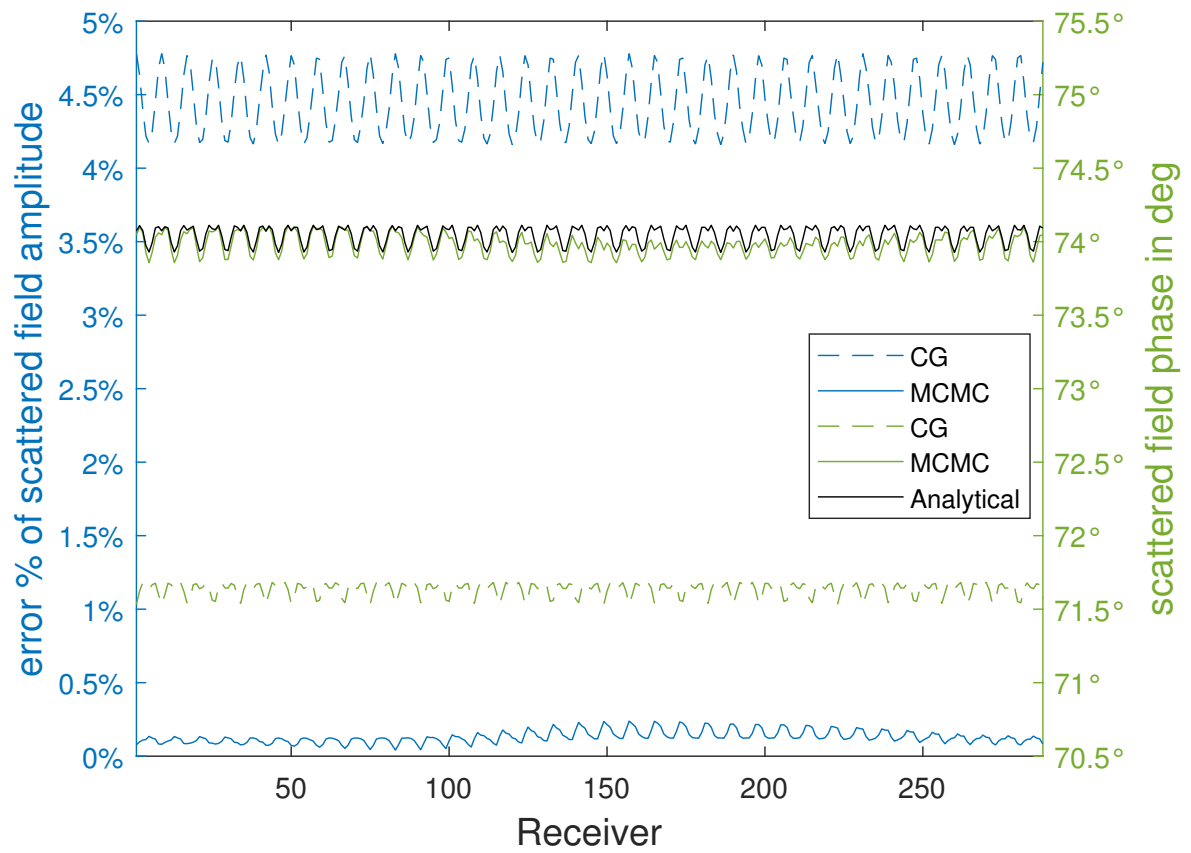


Figure 10: Comparison of scattered fields from the forward model. Left axis: error percentage of amplitude. Right axis: phase.

## CHAPTER 4

### CONVEX OPTIMIZATION

*Part of this chapter was published in IEEE Geoscience and Remote Sensing Letters [3].  
Copyright © CC BY.*

“It is not knowledge, but the act of learning, not possession but the act of getting there, which grants the greatest enjoyment.”

---

Carl Friedrich Gauss

This chapter explores the hidden convexity in inverse scattering problems and solves for unknown permittivity in the wavelet domain. Neither convex optimization [78] nor a wavelet [79] is a stranger in engineering applications. Many techniques target pixel-based inversions, so the number of unknown depends on the pixel number of reconstructed images. To decrease the number of unknowns, the unknowns in the spatial domain can be projected into the sparse wavelet domain but details of non-smooth edges can still be reserved. Wavelet-domain reconstructions was improved in inverse scattering [80], where the unknowns are searched within the wavelet domain and the optimization problem consists of the minimization of the misfit about the data with the sparsity constraints on the wavelet coefficients. To exploit sparsity [81], wavelet transforms, such as Haar and the Daubechies wavelets, have been applied to a wide range

of problems in nonlinear electromagnetic inversions [82]. Also wavelet-based regularizations in DBIM has been applied for MRI [31].

While optimization has been recognized as a useful tool for solving the inverse scattering problem, previous works have not consider nonlinear inverse problems from a convex optimization perspective. Optimization plays a significant role in numerous applications, and convexity is the key to take advantage of reliable and efficient algorithms similar to solving linear equations.

Convex optimization problems exhibit a number of computational benefits because they are a special class of nonlinear optimizations problems. First, every local optimum of a convex optimization problem is also globally optimal; this implies that convex problems can be solved by using efficient local search methods (e.g., Newton's method) as opposed to expensive global methods (e.g., genetic algorithms). With modern solvers specifically designed for convex optimization, a commodity desktop computer can easily handle convex optimization problems up to  $10^3$  to  $10^6$  variables [83], depending on the problem type. Second, in many modern software packages (e.g., CVX [84, 85]) for convex optimization, users can specify convex optimization problems in high-level domain-specific languages. Finally, it is known that convex optimization problems can be solved by solving a sequence of linear systems of equations [86]. This opens the possibility to solve convex problems of very large size by leveraging existing techniques from large-scale numerical linear algebra.

In this chapter, we approximate the nonlinear inverse scattering problem as a convex optimization one by proposing a new inversion strategy consisting of two steps. First, we estimate

the total field inside the domain of investigation by solving a convex optimization problem, which is obtained by discretizing continuous electric field integral equations by the Method of Moment [76]. The solution of the convex optimization problem can be efficiently computed using CVX [84, 85], a software package for solving generic convex optimization problems. Second, the estimated total field is exploited to formulate an inverse problem that reconstructs the dielectric permittivity and conductivity of the target from the scattered field data. To mitigate the ill-posedness of the inverse problem at the second step, we assume that the permittivity profile has a sparse representation in the wavelet domain. This regularizes the inverse problem by introducing an  $\ell_1$ -norm penalty, which is known to promote sparsity in the Haar wavelet coefficients [80]. The resulting problem is known as the LASSO [87] problem and can be solved by the Templates for First-Order Conic Solvers (TFOCS) [88] software package.

The advantage of the first step convex optimization approach is that it does not require the regularization parameter, which is needed by the Born method, and the quality of our results is similar to BIM results. However, the limitation of the first step convex optimization is the effectiveness on electrically large objects. However, the sole second step of using wavelets does not restrict the inversion domain to electrically small regions.

#### 4.1 Theory

Recall that the electromagnetic scattering is governed by a pair of integral equations, Equation 2.11 and Equation 2.12 in Chapter 2. Allow us to review these equations here.

Let  $S$  be the domain under investigation, and  $\mathbf{r}' \in S$ . We denote by  $\epsilon = \epsilon' - j\frac{\sigma}{\omega\epsilon_0}$  the relative complex dielectric permittivity in  $S$ , where  $\epsilon'$  and  $\sigma$  are the relative dielectric permittivity and electrical conductivity.

The state equation accounts for the total field  $E_p$  inside the investigation domain  $S_n$  as Equation 2.12,

$$E_p + \frac{jk_0^2}{4} \sum_{n=1}^N (\epsilon_n - 1) E_n \int_{S_n} \mathrm{H}_0^{(2)}(k_0|\mathbf{r}_p - \mathbf{r}'_n|) \mathrm{d}S' = E_p^i, \quad \mathbf{r}_p \in S, \quad (4.1)$$

where  $E_p^i$  is the incident field at pixel  $p$ ,  $\mathbf{r}_p \in S$ ,  $\mathrm{H}_0^{(2)}(\cdot)$  is the Hankel function of the second kind and order zero,  $k_0$  is the wavenumber in free space. The investigation domain  $S$  is discretized into  $N$  pixels, and  $\epsilon_n$  is the homogeneous relative complex dielectric permittivity within the pixel  $n$ . The integral of  $\mathrm{H}_0^{(2)}(\cdot)$  over a circular region  $S_n$  was evaluated in [76] as Equation 2.13,

$$\begin{aligned} & \frac{jk_0^2}{4} \int_{S_n} \mathrm{H}_0^{(2)}(k_0|\mathbf{r}_p - \mathbf{r}'_n|) \mathrm{d}S' \\ &= \begin{cases} \frac{j\pi k_0 r_{\mathrm{eq}}}{2} \mathrm{H}_1^{(2)}(k_0 r_{\mathrm{eq}}) + 1, & \text{if } p = n \\ \frac{j\pi k_0 r_{\mathrm{eq}}}{2} \mathrm{J}_1(k_0 r_{\mathrm{eq}}) \mathrm{H}_0^{(2)}(k_0|\mathbf{r}_p - \mathbf{r}'_n|), & \text{otherwise} \end{cases} \end{aligned} \quad (4.2)$$

where  $r_{\mathrm{eq}}$  is the equivalent radius of the discretized pixel, and  $\mathrm{J}_1(\cdot)$  is the Bessel function of the first kind and first order.

The data equation describes scattered field  $E^s$  at the  $m$ -th transmitter-receiver combination by Equation 2.11,

$$E_m^s = -\frac{jk_0^2}{4} \sum_{n=1}^N (\epsilon_n - 1) E_n \int_{S_n} H_0^{(2)}(k_0 |\mathbf{r}_m - \mathbf{r}'_n|) dS', \mathbf{r}_m \notin S. \quad (4.3)$$

#### 4.1.1 Approximation with Convex Optimization

A multi-view/multi-static/single-frequency configuration is considered for the problem, same as the configuration in Chapter 2 and Chapter 3. We assume  $N_{\text{TX}}$  transmitters and  $N_{\text{RX}}$  receivers encircling the investigation domain, i.e.,  $N_{\text{TX}}N_{\text{RX}}$  observations of the scattered field.

In inverse scattering problems, both of the permittivity and the electric field in the investigation domain are unknown. Let the vector,  $\epsilon_\delta = \epsilon - 1$ ,  $\epsilon_\delta \in \mathbb{C}^N$ , be the complex contrast function for  $N$  pixels, and the matrix variable  $Y \in \mathbb{C}^{N \times N_{\text{TX}}}$  be the total field at  $N$  pixels due to  $N_{\text{TX}}$  transmitters. These two variables allow us to write Equation 4.3 and Equation 4.1 as

$$A \text{diag}(\epsilon_\delta) Y = D, \quad (4.4)$$

$$Y + B \text{diag}(\epsilon_\delta) Y = C, \quad (4.5)$$

where  $D \in \mathbb{C}^{N_{\text{RX}} \times N_{\text{TX}}}$  consists of the scattered field data  $E_m^s$  in Equation 4.3. The matrices,  $A \in \mathbb{C}^{N_{\text{RX}} \times N}$ ,  $B \in \mathbb{C}^{N \times N}$ , and  $C \in \mathbb{C}^{N \times N_{\text{TX}}}$ , are known once the measurement configuration

and the number of pixels are fixed. Elements of  $A$  relate the scattered field collected at the  $n_{RX}$  receiver to pixel  $p$  as

$$A_{n_{RX},p} = -\frac{j\pi k_0 r_{eq}}{2} J_1(k_0 r_{eq}) H_0^{(2)}(k_0 |\mathbf{r}_{n_{RX}} - \mathbf{r}'_p|). \quad (4.6)$$

Elements of the symmetric matrix  $B$ , given in Equation 4.2, rely on the relationship between pixels  $p$  and  $n$ . The matrix  $C$  accounts for the incident field radiated by a filamentary current in free space, which is expressed at pixel  $p$  for transmitter  $n_{TX}$  as

$$C_{n_{TX},p} = -\frac{k_0^2}{4\omega\epsilon_0} H_0^{(2)}(k_0 |\mathbf{r}_{n_{TX}} - \mathbf{r}'_p|). \quad (4.7)$$

$D_{n_{RX},n_{TX}}$  is the scattered field data at receiver  $n_{RX}$  due to transmitter  $n_{TX}$ .

Before jumping into further steps, assuredly, it is essential to avoid committing any inverse crime. Equation 4.3 and Equation 4.1 can not only produce scattered field data in the forward model but also reveal unknowns in the inverse problem. In the forward model,  $A_{fwd}$ ,  $B_{fwd}$ , and  $\epsilon_{\delta fwd}$  produce  $Y_{fwd}$  and data  $D$ . In the inverse problem,  $A_{inv}$ ,  $B_{inv}$ , and data  $D$  are used to find  $\epsilon_{\delta}$  and  $Y$ . Both of  $A$  and  $B$  depend on the equivalent radius of a pixel,  $r_{eq}$ . If the pixel size kept the same for forward and inverse cases, linear operators in both cases would be identical as  $A_{fwd} = A_{inv}$  and  $B_{fwd} = B_{inv}$ , which result in a “perfectly correct” solution of  $\epsilon_{\delta}$  and  $Y$ . Accordingly, we must discretize the investigation domain into different meshes for forward simulations and inverse problems.

As Equation 4.4 contains the data of the problem, i.e., the observable scattered field, minimizing the difference between the known scattered field data and the computed scattered fields based on proposed permittivity can serve as an objective function. Rather than choose Equation 4.4 as an equality constraints, we minimize the misfit between data and predictions to tolerate potential noise in data. Equation 4.5 relates the field within the scatterer to the permittivity exactly and thus it can serve as an equality constraint. Therefore, a nonconvex optimization problem can be stated from Equation 4.4 and Equation 4.5 as

$$\begin{aligned} \min_{Y, \epsilon_\delta} \quad & \|A \operatorname{diag}(\epsilon_\delta) Y - D\|_2 \\ \text{s.t.} \quad & Y + B \operatorname{diag}(\epsilon_\delta) Y = C. \end{aligned} \tag{4.8}$$

From the exact nonlinear problem as described as Equation 4.8, we start imposing a convex optimization problem. To approximate the nonconvex Equation 4.8, we substitute  $\operatorname{diag}(\epsilon_\delta) Y$  with a new optimization variable,  $Z \in \mathbb{C}^{N \times N_{\text{TX}}}$ , which removes the nonlinearity in the equality constraint by  $Z = \operatorname{diag}(\epsilon_\delta) Y$ . Now, we have a linear optimization formulation

$$\begin{aligned} \min_{Y, Z} \quad & \|A Z - D\|_2 \\ \text{s.t.} \quad & Y + B Z = C. \end{aligned} \tag{4.9}$$

The objective function is a Euclidean norm of an affine function, and the constraint is also affine; therefore, this optimization problem is convex [78]. This convex optimization problem does not require picking appropriate regularization parameters. With CVX, optimal solutions,  $\hat{Y}$  and  $\hat{Z}$ , of our stated convex optimization problem are easily obtained.

To construct convexity, Equation 4.9 relaxes the nonlinear inverse problem and considers the equivalent currents and the total field inside the investigation domain as separate optimization variables. In other words, despite  $Z = \text{diag}(\epsilon_\delta) Y$ ,  $Y$  and  $Z$  are still treated as independent variables to construct the linearity in Equation 4.9.

Due to the nonuniqueness of optimal solutions, CVX would arbitrarily retrieve one solution from the set of optimal solutions and varying constraints do not affect the set of optimal solutions. For any  $Z$ , there exists  $Y$  such that the constraint is satisfied. The inverse source problem, the estimation of  $Z$ , is affected by the inherent non-uniqueness issue as discussed in [89] and [90] that we are trying to estimate a function of spatial variables (defined over a two-dimensional investigation domain) by exploiting the knowledge of the scattered field on a line (one-dimensional domain).

The weakness of approximating the original problem as a convex optimization problem is the absence of the nonconvex constraint of  $Z = \text{diag}(\epsilon_\delta) Y$ . Consequently, solution  $\hat{Z}$  returned by CVX cannot be expressed as the multiplication of a diagonal matrix and the solution  $\hat{Y}$ . The right matrix division,  $\hat{Z}/\hat{Y}$ , returns a sparse matrix with a few non-zero columns instead of a diagonal matrix. Therefore, we only employ the results of the fields in the scatterer,  $\hat{Y}$ , and then solve for the unknown permittivity contrast,  $\epsilon_\delta$  by adopting a LASSO problem in the next step.

#### **4.1.2 Linear Inversions in the Wavelet Domain**

Indeed, coupled with internal field solution  $\hat{Y}$ , Equation 4.4 can be reformulated to highlight the only unknown permittivity contrast  $\epsilon_\delta$ . Although all representations so far are in the

complex domain, we start separating real and imaginary parts of matrices in Equation 4.4 so that everything is in the real domain,

$$\begin{bmatrix} \Re \mathcal{O} & \Im \mathcal{O} \\ \Im \mathcal{O} & -\Re \mathcal{O} \end{bmatrix} \begin{bmatrix} \Re \epsilon_\delta \\ -\Im \epsilon_\delta \end{bmatrix} = \begin{bmatrix} \Re D_{*,1} \\ \vdots \\ \Re D_{*,N_{TX}} \\ \Im D_{*,1} \\ \vdots \\ \Im D_{*,N_{TX}} \end{bmatrix}, \quad (4.10)$$

where the linear complex operator  $\mathcal{O}$  is

$$\mathcal{O} = \begin{bmatrix} A_{1,*} \circ \hat{Y}_{*,1} \\ \vdots \\ A_{N_{RX},*} \circ \hat{Y}_{*,1} \\ A_{1,*} \circ \hat{Y}_{*,2} \\ \vdots \\ A_{N_{RX},*} \circ \hat{Y}_{*,N_{TX}} \end{bmatrix}, \quad (4.11)$$

with element-wise multiplication symbol  $\circ$ , and all elements in a specific row or column omitted by  $*$ . As we transform the complex linear relationship to a real one, the real part of known scattered field vector is cascaded with the imaginary part; similarly, the real part of dielectric permittivity contrast is cascaded with the imaginary one.

Apparently, Equation 4.10 shows a linear form,

$$\mathcal{L} m = d, \quad (4.12)$$

through a linear operator,  $\mathcal{L} \in \mathbb{R}^{2N_{\text{TX}}N_{\text{RX}} \times 2N}$ , between the data,  $d \in \mathbb{R}^{2N_{\text{TX}}N_{\text{RX}}}$ , and the unknown model,  $m \in \mathbb{R}_{\geq 0}^{2N}$ .

To tackle the ill-posedness of the inversion of the underdetermined linear operator  $\mathcal{L}$ , we apply an  $\ell_1$ -norm based regularization method. Because the permittivity profile is either smooth or contains limited sharp features, we assume that once the unknown permittivity parameter is projected in the wavelet domain, numbers of wavelet coefficients is fewer than ones of unknown parameter yet smooth and detail features are reserved. Therefore, the model  $m$  can be unraveled by a linear inverse wavelet transform operator  $\mathcal{W}^{-1}$  and the wavelet coefficients  $w$  as  $m = \mathcal{W}^{-1}w$ . To improve the sparsity, we penalize the misfit between the data and the proposed model with sparse constraints in the wavelet domain, as the LASSO problem was proposed in [87]:

$$\begin{aligned} \min_w \quad & \frac{1}{2} \|\mathcal{L}\mathcal{W}^{-1}w - d\|_2^2 \\ \text{s.t.} \quad & \|w\|_1 \leq \gamma. \end{aligned} \quad (4.13)$$

The parameter  $\gamma$  controls the sparsity of the solution for  $w$ , where the value of  $\gamma$  increases when we consider contrast functions with higher frequency content. The feasible initial point of  $w$  is set as  $w_0 = \mathbf{0}$ . And mathematical symbols in this section can be found in Table II.

TABLE II: KEY SYMBOLS

$\epsilon_\delta$	unknown vector, discretized complex permittivity contrast
$Y$	matrix variable in CVX, electric field in a discretized domain
$\hat{Y}$	solved optimal matrix by CVX, electric field in a discretized domain
$Z$	matrix variable in CVX, $\text{diag}(\epsilon_\delta) Y$
$A$	calculated matrix, proportional to integrals of Green's function
$B$	calculated matrix, proportional to integrals of Green's function
$C$	analytically calculated matrix, incident field by transmitters
$D$	data matrix, scattered field at $N_{RX}$ receivers by $N_{TX}$ transmitters
$d$	data vector, cascading $\Re$ and $\Im$ of all columns of $D$
$\mathcal{O}$	solved complex matrix based on $A$ and $\hat{Y}$
$\mathcal{L}$	solved real matrix formed by $\Re\mathcal{O}$ and $\Im\mathcal{O}$
$m$	unknown vector cascading $\Re\epsilon_\delta$ and $-\Im\epsilon_\delta$
$w$	vector variable in the LASSO problem, wavelet coefficients of $m$
$\gamma$	parameter in the LASSO problem, controlling the sparsity of $w$
$\hat{w}$	solved vector by TFOCS, optimal solution of wavelet coefficients
$\hat{\epsilon}$	solved permittivity, recovered from $\hat{w}$

## 4.2 Numerical Results

In this section, we assess the proposed approach by considering both simulated and experimental data. For the synthetic cases, the investigation domain  $S$  is divided into finer pixels ( $144 \times 144$ ) in the forward model compared to the ones used in the inverse model ( $50 \times 50$ ). The fine grid in the forward model ensures more accurate numerical computations of the scattered field and avoids committing the inverse crime. 8 transmitters and 36 receivers give rise to 288 scattered field data. Transmitters and receivers are located evenly along the circle at 1.5 times the radius of the circular investigation domain  $S$ .

The SDPT3 solver implementing a particular variant of interior-point methods, and called by CVX, costs less than 2 minutes with an Intel Core i7-8700 CPU and 16 GB of RAM for this moderate size problem. In TFOCS, the computation time is within seconds. Overall, it is slower than BIM.

To fully test the effectiveness of our method, we diversify the selection of objects: 1. starting from simplest homogeneous permittivity distribution of a circular cylinder with the known contour; 2. inhomogeneous permittivity distribution with of a circular cylinder with the known contour; 3. homogeneous permittivity distribution with unknown contour.

### 4.2.1 A Homogeneous Circular Cylinder: Lossless and Lossy

#### 4.2.1.1 A Lossless Homogeneous Cylinder: $\epsilon = 11$

In this case, we test our method along with the BIM method. The domain of investigation has a homogeneous permittivity distribution of  $\epsilon = 11$ . First, we follow the case of Figure 6 in [52] of a circular cylinder with a radius of  $\lambda/20$ . In BIM, the total field within the

cylinder  $E_n^{\text{BIM}}$  is achieved after 14 iterations with relative residual error less than  $10^{-4}$ . The regularization method for the inversion is the algebraic reconstruction technique [91], instead of the Tikhonov regularization in [52]. The total field estimated by proposed convex optimization method is  $E_n^{\text{CVX}}$ . Figure 11 shows the relative complex error for the total field,

$$\delta^{\text{BIM,CVX}} = \frac{E_n^{\text{Analytical}} - E_n^{\text{BIM,CVX}}}{|E_n^{\text{Analytical}}|}, \quad (4.14)$$

at each pixel of the investigation domain, when the transmitter is located at  $(0, 1.5\lambda/20)$ . Neither approximations nor a priori knowledge are used, but CVX attains a better reconstruction of the total field, especially for the real part of  $E_n$ .

Then we examine the permittivity distribution by BIM and the proposed CVX-TFOCS method. By BIM as shown in Figure 12a, the mean of reconstructed permittivity 10.8889, and the variance is 0.8746; by CVX-TFOCS, the mean of reconstructed permittivity 10.9956, and the variance is 0.014 in Figure 12b. Both Figure 12a and Figure 12b share the same colorbar to the right. Due to more accurate estimates of  $E_n$  by CVX and the sparse nature of a homogeneous permittivity distribution, the LASSO solution enables a clean reconstruction.

Also, it has been observed that a good performance of the proposed approach also for even larger value of relative dielectric permittivity with radius  $\lambda/20$ :  $\frac{\|E_n^{\text{CVX}} - E_n^{\text{Analytical}}\|_2}{\|E_n^{\text{SIM}}\|_2} = 1.08\%$  for  $\epsilon = 15$ ,  $0.74\%$  for  $\epsilon = 20$ , and  $9.8\%$  for  $\epsilon = 40$ .

After, we assess the performance of CVX with larger objects, such as radius of  $\lambda/8$ ,  $\lambda/4$ , and  $\lambda/2$ . The permittivity estimated along the slice of  $y = 0$  by BIM and CVX-TFOCS is

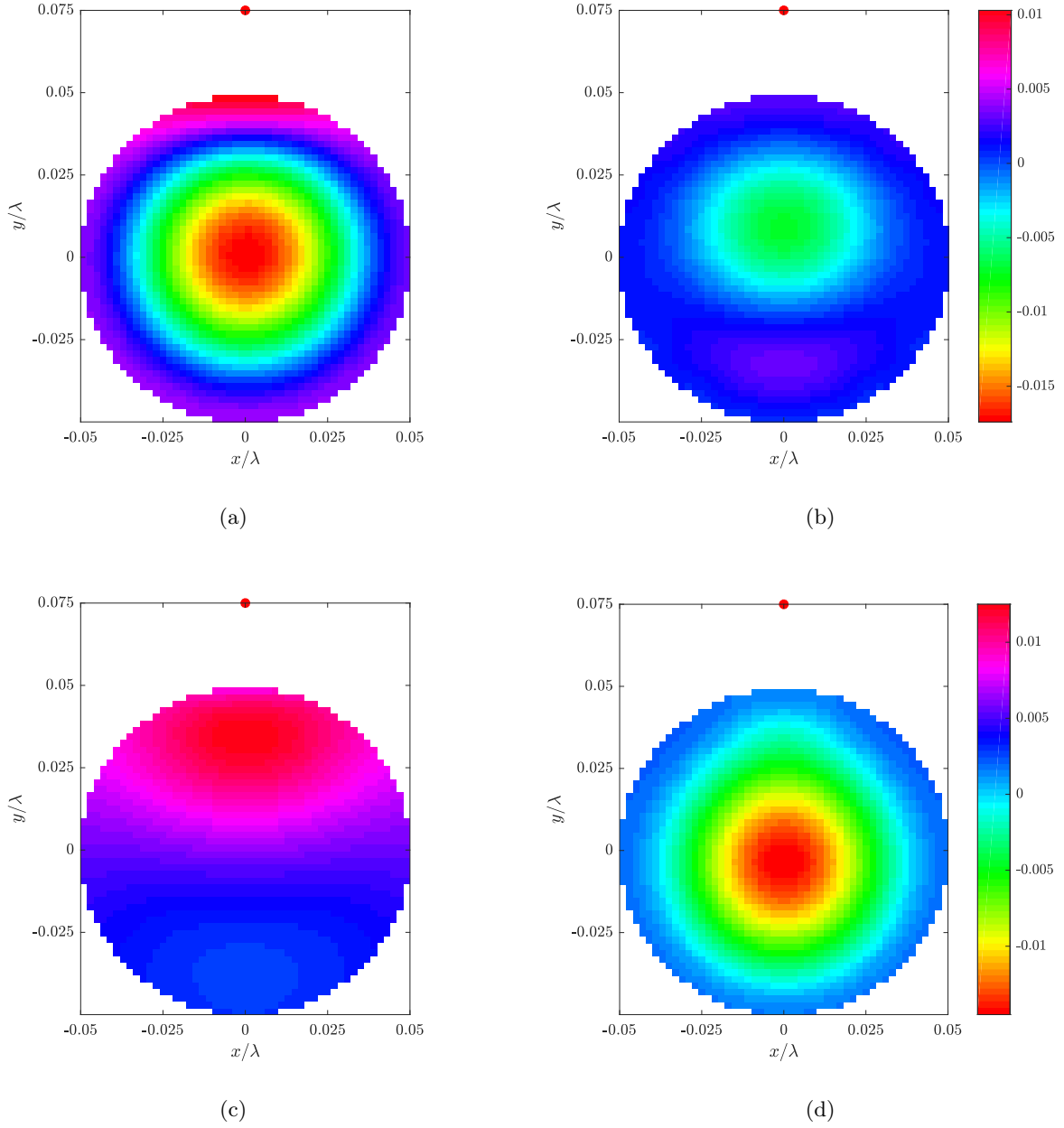


Figure 11: Electric field relative error within the cylinder with  $\epsilon = 11$ : (a)  $\mathfrak{R}\delta^{\text{BIM}}$ ; (b)  $\mathfrak{R}\delta^{\text{CVX}}$ ; (c)  $\Im\delta^{\text{BIM}}$ ; (d)  $\Im\delta^{\text{CVX}}$ . The red dot at  $(0, 0.075\lambda)$  shows the location of the transmitter. Results on the same row share the colorbar on the right.

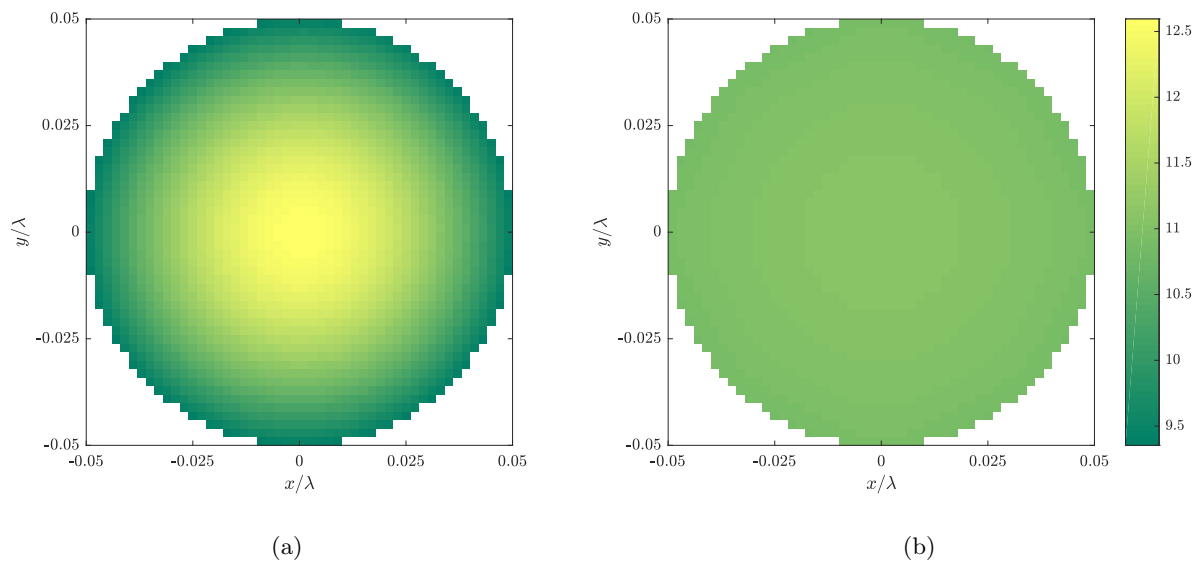


Figure 12: Permittivity reconstruction of the cylinder with  $\epsilon = 11$  by: (a) BIM; (b) CVX-TFOCS.

Results share the colorbar on the right.

shown in Figure 13. Based on the discretization rule in [76], with  $50 \times 50$  pixels, the edge dimension of each cell for an object with the radius  $\lambda/2$  is  $\lambda/50$ , which does not exceed the criterion  $0.2/\sqrt{11}\lambda$ . Figure 13 shows, in this case, the larger extent of the targets entails a worse quality of approximation of the total field, which leads to worse permittivity reconstruction.

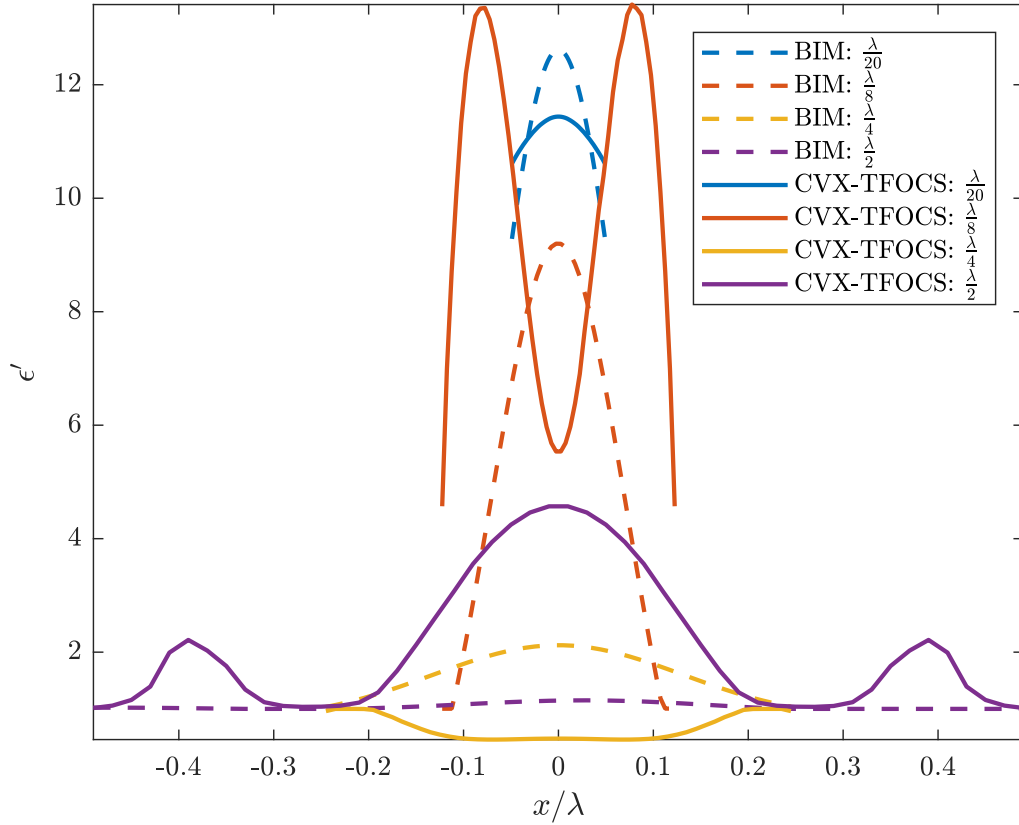


Figure 13: Real part of permittivity reconstructed along  $y = 0$  by BIM and CVX-TFOCS for a circular cylinder with permittivity 11 with varying radius,  $\lambda/20$ ,  $\lambda/8$ ,  $\lambda/4$ , and  $\lambda/2$ .

#### 4.2.1.2 A Lossy Homogeneous Cylinder: $\epsilon = 2 - 1j$

The domain of investigation is a lossy homogeneous cylinder with  $\epsilon = 2 - 1j$ , i.e.  $\sigma = 0.0556$ , and the radius is  $\lambda/4$ . Figure 14 shows reconstructed results of the complex permittivity. The mean of reconstructed permittivity is  $1.9201 - 1.1489j$ , and the variance is 0.0046. The reconstructed permittivity shows more variance for this lossy case than the lossless Figure 12b.

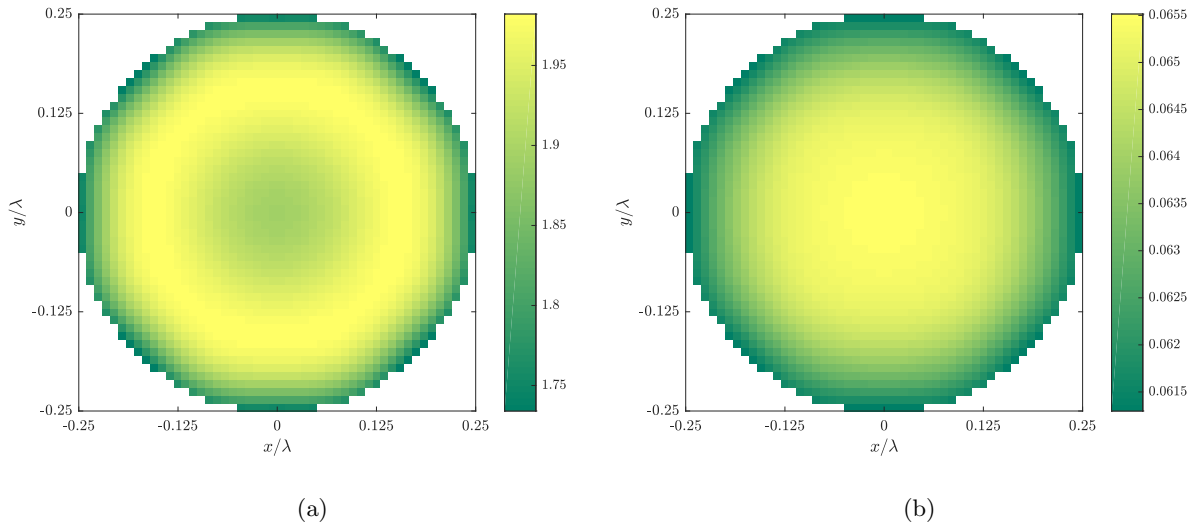


Figure 14: Permittivity reconstruction of the cylinder  $\epsilon = 2 - 1j$ , i.e.  $\sigma = 0.0556$ : (a) real part; (b) conductivity.

## 4.2.2 An Inhomogeneous Circular Cylinder

### 4.2.2.1 A Sine Shape Distribution

The sine-shaped permittivity distribution reaches to the maximum of 3 at  $(0, 0)$  and the minimum of 1 at the edge with the radius of  $\lambda/4$ . To test the robustness of our method, we add the white Gaussian noise,  $\tilde{N} \sim \mathcal{N}(0, \sigma^2/2)$  (here  $\sigma$  is the variance instead of the symbol of conductivity), to the real and imaginary part of scattered field data  $\tilde{S}$ . With the signal-to-noise ratio (SNR),

$$\text{SNR} = 10 \log \frac{\text{Power}(\tilde{S})}{\sigma^2}, \quad (4.15)$$

the scattered field for the sine-shaped object altered with a 30 dB SNR.

First, the reconstructed electric field obtained in CVX is compared between the noiseless and the noisy case. Figure 15 shows the relative error of the reconstructed field at each pixel when the transmitter locates at  $(0, 1.5\lambda/4)$ . The maximum imaginary error is boosted up with noise, because the real part of the data contributes more to the power, and we use the same power level when adding the noise to the real and the imaginary part; in another words, relatively more noise is added to the imaginary part of the data. The noise from a 30 dB SNR is not very strong, however, the result by CVX is disturbed with less than 50% error. This might suggest a lack of robustness in our method.

Figure 16 shows the pixel-based reconstructed permittivity. With the added noise, the maximum values of reconstructed permittivity go further than the noiseless case. However, for both cases, the reconstructions of the imaginary part are quite accurate.

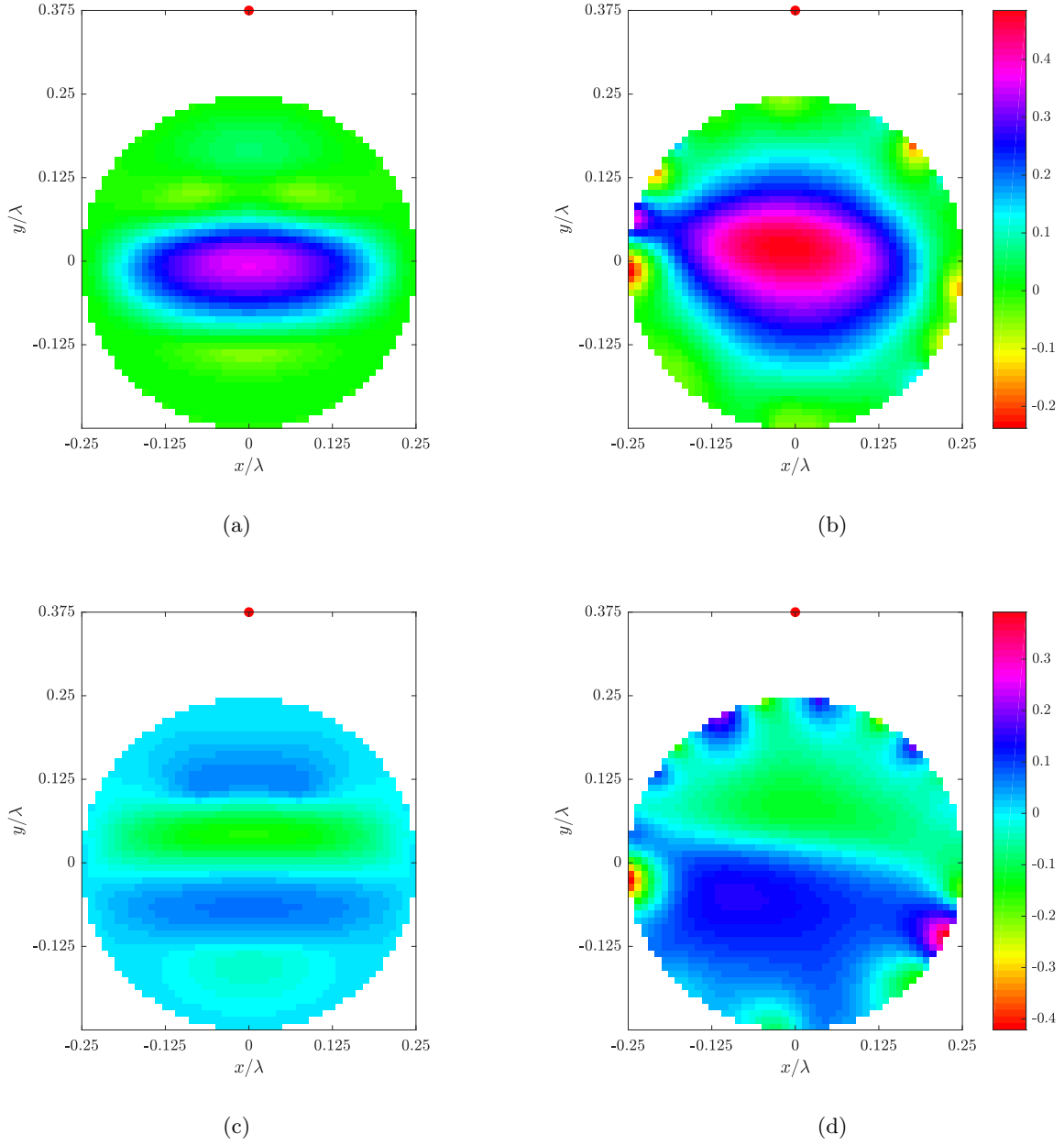


Figure 15: Relative error of electric field for the sine-shaped distribution: (a)  $\Re\delta^{\text{Noiseless}}$ ; (b)  $\Re\delta^{30 \text{ dB}}$ ; (c)  $\Im\delta^{\text{Noiseless}}$ ; (d)  $\Im\delta^{30 \text{ dB}}$ . The red dot at  $(0, 0.375\lambda)$  shows the location of the transmitter. Results on the same row share the colorbar on the right.

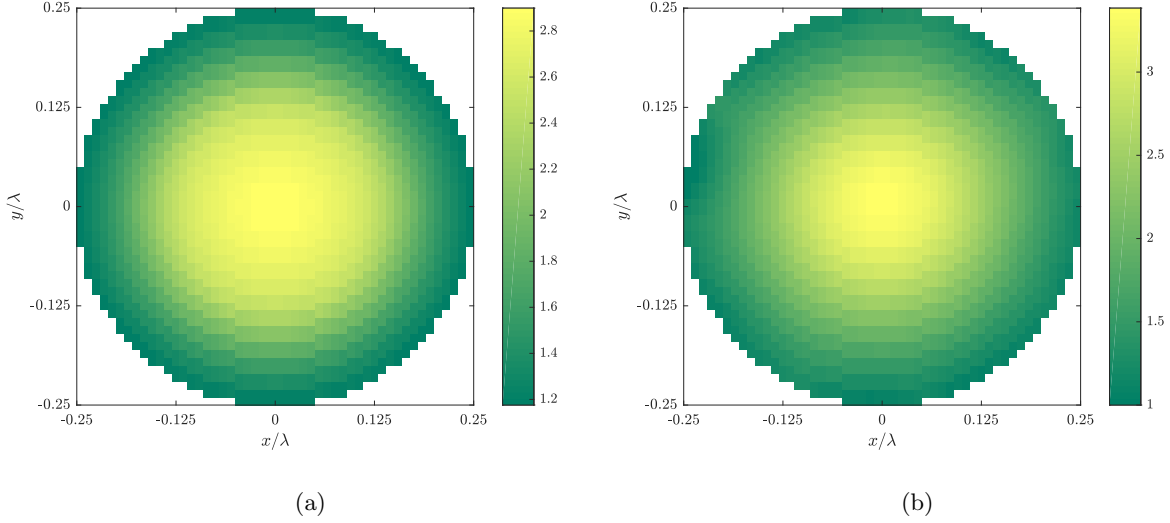


Figure 16: Reconstructed real part of permittivity within a sine-shaped permittivity distribution with maximum  $\epsilon = 3$  at  $(0,0)$  and the minimum of 1 at the edge: (a) noiseless; (b) 30 dB SNR.

Then, we decrease the SNR of the scattered field to 20 dB. Figure 17b shows the reconstructed permittivity compared to the actual object in Figure 17a.

#### 4.2.2.2 A Layered Cylinder

For a lossless layered cylinder, the outer layer has the permittivity of  $\epsilon = 4$  and the inner layer has the permittivity of  $\epsilon = 2$ . the radius of the outer layer is  $0.25\lambda$ , and the radius of the inner layer is  $0.15\lambda$ . Figure 18a shows reconstructed permittivity with noiseless electric field and Figure 18b with the SNR of 20dB. The homogeneous spatial behavior and the permittivity value for the outer layer are well estimated, whereas there is a smoothly varying distribution for the inner layer.

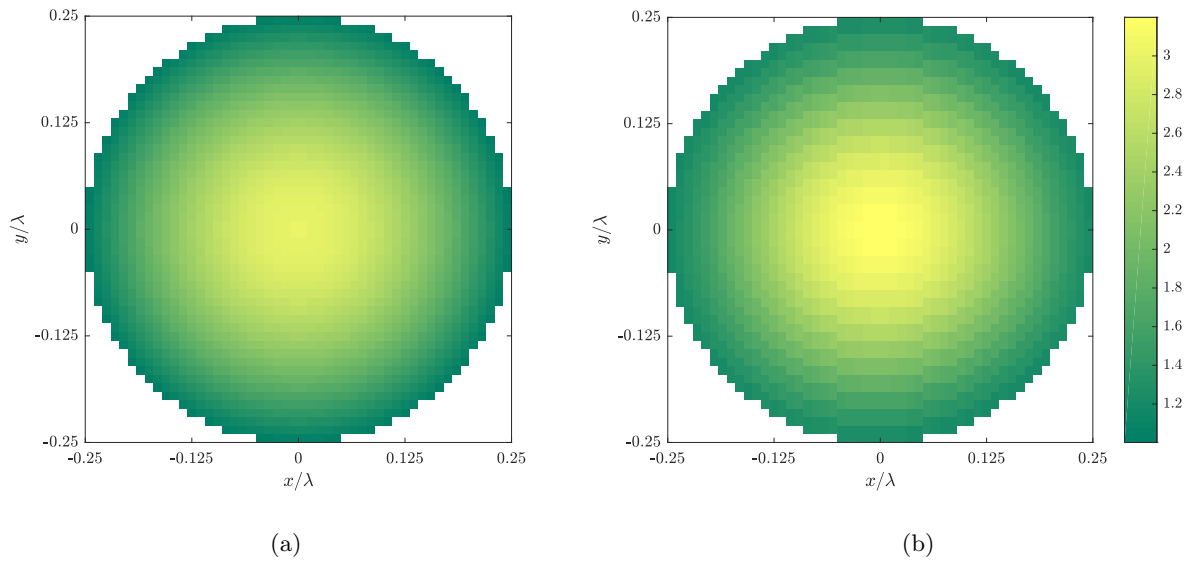


Figure 17: Real part of permittivity within a sine-shaped permittivity distribution with maximum  $\epsilon = 3$  at  $(0,0)$  and the minimum of 1 at the edge: (a) actual; (b) reconstructed with a 20 dB SNR. Results share the colorbar on the right.

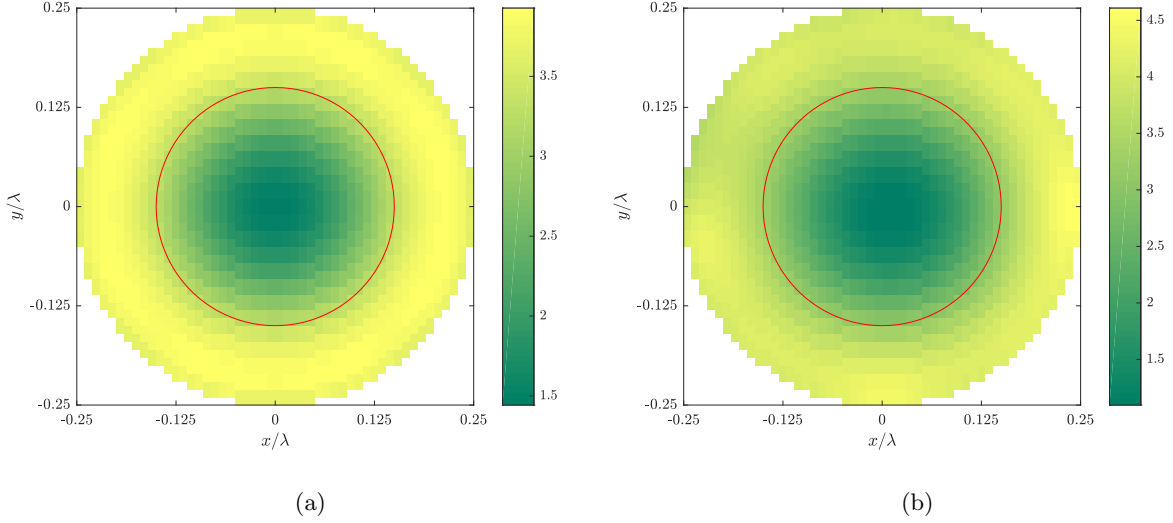


Figure 18: Reconstructed permittivity of a layered cylinder, the red line indicates the actual boundary between the outer layer with  $\epsilon = 4$  and the inner layer with  $\epsilon = 2$ : (a) noiseless; (b) 20dB SNR.

### 4.2.3 Detection of Shape and Dielectric Properties

#### 4.2.3.1 L-shaped Plexiglass

The L-shaped plexiglass with  $\epsilon = 2.6$  is placed in the investigation domain of  $\lambda/2$ . For noiseless electric field data, Figure 19a shows a good identification of the L-shape and a clean  $\epsilon = 1$  for the rest of the investigation domain. The reconstructed permittivity within the plexiglass also lies within acceptable range. Figure 19b shows that the L-shape is clearly identified and that the remaining area of the investigation domain also has a clean  $\epsilon = 1$  almost everywhere.

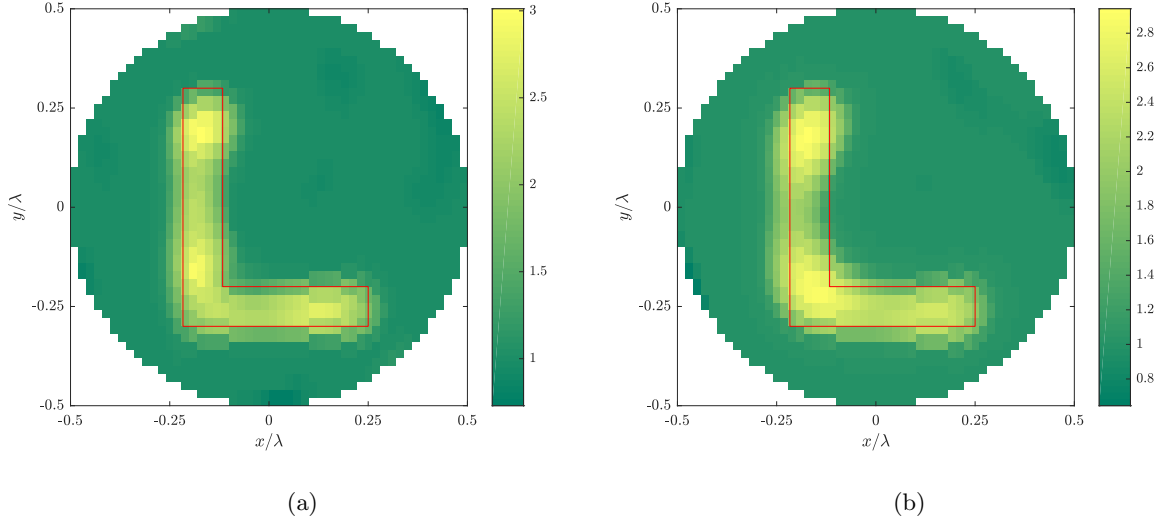


Figure 19: Reconstructed permittivity of an L-shaped plexiglass with  $\epsilon = 2.6$ : (a) noiseless; (b) 20dB SNR.

#### 4.2.3.2 Two High Density Polyethylene Cylinders from Measurement

We apply the proposed method to the experimental data presented in [48]. 15 transmitter locations were uniformly assigned along an arc of  $280^\circ$  with a radius of 0.432 m; 80 receiver locations were along a full circular orbit of radius 0.328 m. The transmitter and the receiver were log-periodic antennas (Ramsey Model No. LPY26) at 5 GHz. An automatic antenna positioning system programmed in LabView was connected with a vector network analyzer (HP 8753ES), and measured  $S_{21}$  data were interpreted into scattered field data.

Two high-density polyethylene (HDPE) cylinders with a relative permittivity  $\epsilon = 2.26$  are located in the domain of investigation with radius  $\lambda$ . The cylinders have a radius of 0.0127 m ( $0.21 \lambda$ ) and the minimal distance between them is 0.02 m ( $0.33 \lambda$ ). First, reconstructed permittivity is shown in Figure 20a when a quadratic inverse model in [48] is used. The boundaries are smooth and the maximum permittivity is 1.7823. Figure 20b presents the reconstructed permittivity by CVX-TFOCS. Two detected targets have a more accurate permittivity and most of the background area has a correctly estimated value of permittivity  $\epsilon = 1$ .

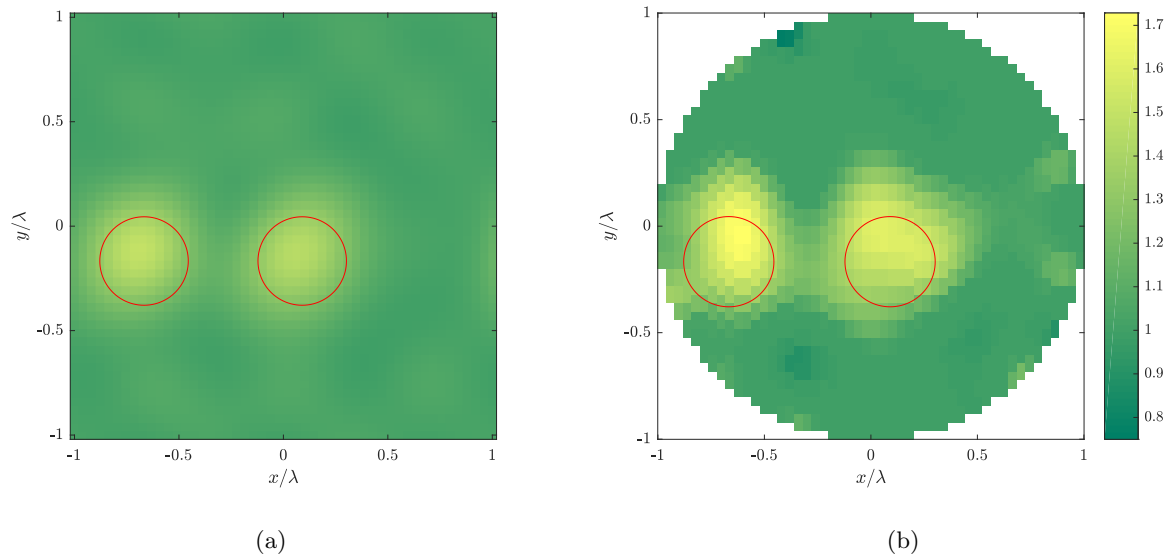


Figure 20: Reconstructed permittivity of two HDPE cylinders with  $\epsilon = 2.26$ : (a) quadratic model; (b) CVX-TFOCS. The red circles indicate the contour of the original cylinders. Results share the colorbar on the right.

### 4.3 Discussion

We proposed a two-step strategy based on a convex optimization scheme and a LASSO scheme in the wavelet domain for solving an inverse scattering problem. After, we present a validation of the method with both simulated and experimental data. Without a priori knowledge or tuning regularization parameters, CVX estimates total field information well for objects with relatively small electric size and shows robustness when noise is present. Future developments should analyze theoretically the performance in the case of larger investigation domains [92] and propose more tractable constraints on this optimization problem.

## CHAPTER 5

### CONCLUDING REMARKS

#### 5.1 Summary

In the past, nonlinear inverse scattering problems could be linearized with the Born approximation and solved iteratively by minimizing a cost function that consists of norms.

In Chapter 3, we combined the Born iterative method (BIM) and stochastic optimization strategies. The first step deterministic approach is based on the BIM stabilized by regularization techniques, Algebraic Reconstruction Technique (ART) and Conjugate Gradient (CG). In the second step, either genetic algorithm (GA) or Bayesian inference solved by Monte Carlo Markov chain is carried out. The whole idea depends on the hope of BIM results acting as the priori knowledge of the second step stochastic method, which shows limited improvements with high computational cost compared with the first step BIM results. The test cases are weak and homogenous, strong and homogeneous, and layered permittivity.

In Chapter 4, our attempt aims to approximate the nonlinear inverse scattering problem without the Born approximation and reduce the effects of choosing tuning parameters in regularizations of BIM. Under the convex optimization regime, we proposed a simple convex approximation of discrete inverse scattering problems for the unknown internal field inside the investigation domain. This reformulation abandons approximations and priori knowledge, yet enables direct and efficient estimates of unknown electric field and saves computational resources

compared with metaheuristic optimizations and stochastic methods. Then, these internal field results linearize the inverse problem for permittivity, and the reconstruction of wavelet coefficients for the unknown permittivity exploits the sparsity of the solution, and reconstructions from simple level 1 Haar wavelet domain preserve fair details on sharp edges. The combination of convex optimization and wavelets coefficients offer satisfying results on our limited test cases. We tested our method with strong and lossless homogeneous, lossy homogeneous, inhomogeneous but smooth, or not smooth permittivity distribution, from both simulated data (noiseless and noisy) and real experimental measurements. The limitation of the convex optimization perspective is the lack of robustness when dealing with noise. In the future, improving robustness of this method or investigation on optimal solutions could be explored.

Overall, the convex optimization approximation and wavelet-based optimization outperforms the combination of the BIM and the stochastic method due to higher accuracy and lower computational cost.

## 5.2 Future Directions

The weakness of approximating the original problem as a convex optimization problem is the absence of the nonconvex constraint of  $Z = \text{diag}(\epsilon_\delta) Y$ . Consequently, solution  $\hat{Z}$  returned by CVX cannot be expressed as the multiplication of a diagonal matrix and the solution  $\hat{Y}$ . To estimate the permittivity contrast  $\epsilon_\delta$ , we used the estimated total field,  $\hat{Y}$ , and adopt a LASSO problem at the second step.

One direction could be to get  $\epsilon_\delta$  directly from  $\hat{Y}$  and  $\hat{Z}$ : either minimizing the unconstrained  $\ell_2$  norm

$$\min_{\epsilon_\delta} \|\hat{Z} - \text{diag}(\epsilon_\delta) \hat{Y}\|_2, \quad (5.1)$$

or in the wavelet domain

$$\begin{aligned} \min_w \quad & \|\hat{Z} - \text{diag}(\mathcal{W}^{-1}w) \hat{Y}\|_2 \\ \text{s.t.} \quad & \|w\|_1 \leq \gamma. \end{aligned} \quad (5.2)$$

Another direction is to solve nonlinear least-squares with proximal Newton's method [93,94].

## APPENDICES

## Appendix A

### ELECTRIC FIELD INTEGRAL EQUATION

An electric field integral equation (EFIE) is the core mathematical representation of scattering problems. In this appendix, we show key components of EFIEs. First, we derive the kernel function of the electric field integral equation, i.e. the Green's function, which is the solution to vector wave equations. Then, with the volume equivalence theorem, we describe the 3D and the 2D electromagnetic scattering phenomena and then introduce the electric field integral equation. The IEEE time convention  $e^{j\omega t}$  is assumed.

#### A.1 Green's Function as the Solution to the Vector Wave Equations

Maxwell's equations outline the foundation of electromagnetics by relating the electric field and the magnetic field with any source and medium. No matter looking for the electric field or the permittivity, we need to start from procedures of solving these partial differential equations.

The time harmonics form or the phasor representation of Maxwell's equations are

$$\nabla \times \mathbf{E}(\mathbf{r}) = -j\omega\mu(\mathbf{r})\mu_0\mathbf{H}(\mathbf{r}) - \mathbf{M}(\mathbf{r}), \quad (\text{A.1a})$$

$$\nabla \times \mathbf{H}(\mathbf{r}) = j\omega\epsilon(\mathbf{r})\epsilon_0\mathbf{E}(\mathbf{r}) + \mathbf{J}(\mathbf{r}), \quad (\text{A.1b})$$

$$\nabla \cdot \mathbf{E}(\mathbf{r}) = \frac{\rho}{\epsilon(\mathbf{r})\epsilon_0}, \quad (\text{A.1c})$$

$$\nabla \cdot \mathbf{H}(\mathbf{r}) = 0, \quad (\text{A.1d})$$

## Appendix A (Continued)

where  $\mathbf{E}$  is the electric field,  $\mathbf{H}$  is the magnetic field,  $\epsilon_0$  is the permittivity in free space,  $\epsilon$  is the relative permittivity of the medium,  $\mu_0$  is the permeability in free space,  $\mu$  is the relative permeability of the medium  $\mathbf{M}$  is the magnetic current density,  $\mathbf{J}$  is the electric current density,  $\rho$  is the total electric charge density,  $\omega$  is the wave radial frequency. These are the also the Fourier transform of the time-domain Maxwell's equations.

In digital signal processing or control theory, the impulse response can characterize a system since it is equivalent to the inverse Laplace transform of the system's transfer function. Similarly, Green's function can characterize the potential generated by a unit amplitude point source. Considering the vector wave equation,

$$\nabla \times \nabla \times \mathbf{E}(\mathbf{r}) - k^2 \mathbf{E}(\mathbf{r}) = -j\omega\mu_0 \mathbf{J}(\mathbf{r}), \quad (\text{A.2})$$

the electric field due to the current density source is the superposition of all point sources in space as

$$\mathbf{E}(\mathbf{r}) = j\omega\mu_0 \int_V \overline{\mathbf{G}}(\mathbf{r}, \mathbf{r}') \cdot \mathbf{J}(\mathbf{r}') dV', \quad (\text{A.3})$$

where  $\overline{\mathbf{G}}(\mathbf{r}, \mathbf{r}')$  is the Dyadic Green's function. This Green's function acts as the point source response of the vector wave equation Equation A.2,

$$\nabla \times \nabla \times \overline{\mathbf{G}}(\mathbf{r}, \mathbf{r}') - k^2 \overline{\mathbf{G}}(\mathbf{r}, \mathbf{r}') = -\overline{\mathbf{I}}\delta(\mathbf{r}, \mathbf{r}'), \quad (\text{A.4})$$

## Appendix A (Continued)

and the solution is given by Tai [95],

$$\overline{\mathbf{G}}(\mathbf{r}, \mathbf{r}') = -(\overline{\mathbf{I}} + \frac{1}{k^2} \nabla \nabla) \frac{e^{-jk|\mathbf{r}-\mathbf{r}'|}}{4\pi|\mathbf{r}-\mathbf{r}'|}. \quad (\text{A.5})$$

### A.2 Volume Equivalence Principle and Scattering

An electric current density  $\mathbf{J}(\mathbf{r})$  in free space generates the incident electric field  $\mathbf{E}^i(\mathbf{r})$  and the magnetic field  $\mathbf{H}^i(\mathbf{r})$  as

$$\nabla \times \mathbf{E}^i(\mathbf{r}) = -j\omega\mu_0\mathbf{H}^i(\mathbf{r}), \quad (\text{A.6a})$$

$$\nabla \times \mathbf{H}^i(\mathbf{r}) = j\omega\epsilon_0\mathbf{E}^i(\mathbf{r}) + \mathbf{J}(\mathbf{r}). \quad (\text{A.6b})$$

In the presence of an obstacle,  $V$ , these radiating current density densities  $\mathbf{J}(\mathbf{r})$  and  $\mathbf{M}(\mathbf{r})$  satisfy

$$\nabla \times \mathbf{E}(\mathbf{r}) = -j\omega\mu(\mathbf{r})\mu_0\mathbf{H}(\mathbf{r}) - \mathbf{M}(\mathbf{r}), \quad (\text{A.7a})$$

$$\nabla \times \mathbf{H}(\mathbf{r}) = j\omega\epsilon(\mathbf{r})\epsilon_0\mathbf{E}(\mathbf{r}) + \mathbf{J}(\mathbf{r}), \quad (\text{A.7b})$$

where  $\mu(\mathbf{r})$  and  $\epsilon(\mathbf{r})$  are the relative inhomogeneous permeability and permittivity. Substrating Equation A.6 from Equation A.7, one obtains the scattered fields

$$\nabla \times \mathbf{E}^s(\mathbf{r}) = -j\omega\mu_0\mathbf{H}^s(\mathbf{r}) - \mathbf{M}_{\text{eq}}(\mathbf{r}), \quad (\text{A.8a})$$

$$\nabla \times \mathbf{H}^s(\mathbf{r}) = j\omega\epsilon_0\mathbf{E}^s(\mathbf{r}) + \mathbf{J}_{\text{eq}}(\mathbf{r}), \quad (\text{A.8b})$$

## Appendix A (Continued)

where the equivalent sources  $\mathbf{M}_{\text{eq}}(\mathbf{r})$  and  $\mathbf{J}_{\text{eq}}(\mathbf{r})$  are a function of the contrast between the obstacle and the background medium,

$$\mathbf{M}_{\text{eq}}(\mathbf{r}) = j\omega\mu_0(\mu(\mathbf{r}) - 1)\mathbf{H}(\mathbf{r}), \quad (\text{A.9a})$$

$$\mathbf{J}_{\text{eq}}(\mathbf{r}) = j\omega\epsilon_0(\epsilon(\mathbf{r}) - 1)\mathbf{E}(\mathbf{r}). \quad (\text{A.9b})$$

When  $\mathbf{M}_{\text{eq}}(\mathbf{r}) = 0$ , the equivalent current source  $\mathbf{J}_{\text{eq}}(\mathbf{r})$  is linked with the scattered electric field by the dyadic Greens function that

$$\mathbf{E}^{\text{s}}(\mathbf{r}) = j\omega\mu_0 \int_V \overline{\mathbf{G}}(\mathbf{r}, \mathbf{r}') \cdot \mathbf{J}_{\text{eq}}(\mathbf{r}') dV', \quad (\text{A.10})$$

and the total field is the summation of the incident and the scattered field

$$\mathbf{E}(\mathbf{r}) = \mathbf{E}^{\text{i}}(\mathbf{r}) - k_0^2 \int_V (\epsilon(\mathbf{r}') - 1) \overline{\mathbf{G}}(\mathbf{r}, \mathbf{r}') \cdot \mathbf{E}(\mathbf{r}') dV'. \quad (\text{A.11})$$

### A.3 Two Dimensional Electric Field Integral Equation

Consider the two dimensional electromagnetic scattering problem shown in Figure 1. An infinitely long cylinder with arbitrary cross section is illuminated by a  $\text{TM}^z$ -mode line electric source. Such a source transmits the electric field that is uniform along  $\hat{z}$ , and the scattered

## Appendix A (Continued)

field and the total field are also invariant of  $z$  because of symmetry, i.e.  $\mathbf{E}(\mathbf{r}) = E(\mathbf{r}_{2D})\hat{z}$  with  $\mathbf{r} = \mathbf{r}_{2D} + \hat{z}$ . And Equation A.11 can be rewritten as

$$\begin{aligned} E(\mathbf{r}_{2D}) &= E^i(\mathbf{r}_{2D}) - k_0^2 \int_S \int_{-\infty}^{\infty} (\epsilon(\mathbf{r}'_{2D}) - 1) \overline{\mathbf{G}}(\mathbf{r}, \mathbf{r}') E(\mathbf{r}'_{2D}) dz dS' \\ &= E^i(\mathbf{r}_{2D}) - k_0^2 \int_S (\epsilon(\mathbf{r}'_{2D}) - 1) E(\mathbf{r}'_{2D}) \int_{-\infty}^{\infty} \overline{\mathbf{G}}(\mathbf{r}, \mathbf{r}') dz dS'. \end{aligned} \quad (\text{A.12})$$

Then two dimensional Green's function is the integral over  $z$  in Equation A.12 and based on [32], one plugs Equation A.5 of the Green's function and has

$$\begin{aligned} G_{2D}(\mathbf{r}_{2D}, \mathbf{r}'_{2D}) &= \int_{-\infty}^{\infty} \overline{\mathbf{G}}(\mathbf{r}, \mathbf{r}') dz \\ &= \int_{-\infty}^{\infty} -(\bar{\mathbf{I}} + \frac{1}{k^2} \nabla \nabla) \frac{e^{-jk|\mathbf{r}-\mathbf{r}'|}}{4\pi|\mathbf{r}-\mathbf{r}'|} dz \\ &= -(\bar{\mathbf{I}} + \frac{1}{k^2} \nabla \nabla) \int_{-\infty}^{\infty} \frac{e^{-jk|\mathbf{r}-\mathbf{r}'|}}{4\pi|\mathbf{r}-\mathbf{r}'|} dz \\ &= (\bar{\mathbf{I}} + \frac{1}{k^2} \nabla \nabla) \frac{j}{4} H_0^{(2)}(k_0|\mathbf{r}-\mathbf{r}'|) \\ &= \frac{j}{4} H_0^{(2)}(k_0|\mathbf{r}_{2D}-\mathbf{r}'_{2D}|). \end{aligned} \quad (\text{A.13})$$

Therefore, the 2D electric field integral equation can be obtained as

$$E(\mathbf{r}_{2D}) = E^i(\mathbf{r}_{2D}) - \frac{jk_0^2}{4} \int_S (\epsilon(\mathbf{r}'_{2D}) - 1) E(\mathbf{r}'_{2D}) H_0^{(2)}(k_0|\mathbf{r}_{2D}-\mathbf{r}'_{2D}|) dS', \quad (\text{A.14})$$

where  $H_0^{(2)}$  is the Hankel function of the second kind of order zero.

## Appendix A (Continued)

### A.4 Fredholm Equations

The Fredholm equation was originally studied by Erik Ivar Fredholm; in the Fredholm theory, the infinite Liouville–Neumann series are one technique of solving the Fredholm integral equations. The difference between the first kind and the second kind is the location of the unknown function that one needs to solve.

A Fredholm equation of the first kind is written as

$$\phi(t) = \int K(t, s)f(s) ds, \quad (\text{A.15})$$

where the kernel function  $K(t, s)$  and the function  $\phi(t)$  are given, while the function that needs to be find,  $f(t)$ , is in the integrand. This can be related to the inverse scattering problem stated as Equation A.14 when  $\mathbf{r} \notin S$ : the total field and incident field are known, while the unknown permittivity only appears within the integrand.

A Fredholm equation of the second kind is given as

$$f(t) = \phi(t) + \lambda \int K(t, s)f(s) ds. \quad (\text{A.16})$$

On the contrary,  $f(t)$ , the unknown of the second kind appears not only in the integrand but also outside the integrand. This describes the forward problem for the internal electric field of the investigation domain as in Equation A.14 when  $\mathbf{r} \in S$ : in the integrand, unknown is the internal field since the permittivity profile  $\epsilon$  is given; however, the unknown internal field also

## Appendix A (Continued)

lies outside the integrand. Thus, this Fredholm integral equation of the second kind is strongly connected with the forward scattering problem.

## Appendix B

### FORWARD PROBLEM SOLVER - METHOD OF MOMENT

Both forward and inverse scattering problems can be discretized with the Method of Moment (MoM). We coded the MoM solver described as [76] in MATLAB, and we believe that any acclaimed achievements could be the hanging gardens in Babylon unless the solver is properly validated. Therefore, this appendix compares the numerical results from the MoM solver with results in [76].

#### **B.1 An Elevation Pitch for Method of Moment**

Here we focus on the descriptive introduction of MoM; therefore, the detailed mathematical representation can be found in [76] or Chapter 2.2.3.

The problem setup is as follows: there is an infinitely long cylinder, let us say the cylinder is aligned along the  $\hat{z}$  and has the same cross section, which means its dimension on the  $xy$ -plane is not a function of  $\hat{z}$ . So the shape of the cross section and its dielectric property are known. Now this object is illuminated by either a TM-mode line source that is parallel with it, or a plane wave that propagates vertical to  $\hat{z}$ .

Given the cross section and the dielectric properties of any infinitely long object that is illuminated by either TM-mode line source or a plane wave, the goal is to calculate the internal total field in the object and the scattered field outside the object.

## Appendix B (Continued)

It is assumed that, in each pixel, the permittivity is considered as homogeneous. Therefore, the discretized pixel size should be sufficiently small: the edge of the pixel should not exceed  $0.2\lambda/\sqrt{\epsilon}$  as suggested in [76]. However, the assumption of constant dielectric property and electric field within in a pixel also causes some limitation to application to high conductive objects. For example, for perfectly conducting objects, we know that the electric field inside is zero.

Figure 21 shows the geometry of a ring cylinder with a lossless permittivity of 4, the outer radius is  $0.3 \lambda$ , and the inner radius is  $0.25 \lambda$ . The ring is illuminated by either a plane wave or a line source. The results from MATLAB MoM codes as shown in Figure 22 and also match with original results from [76]; therefore, these MoM codes are verified and used for forward models throughout this work.

## Appendix B (Continued)

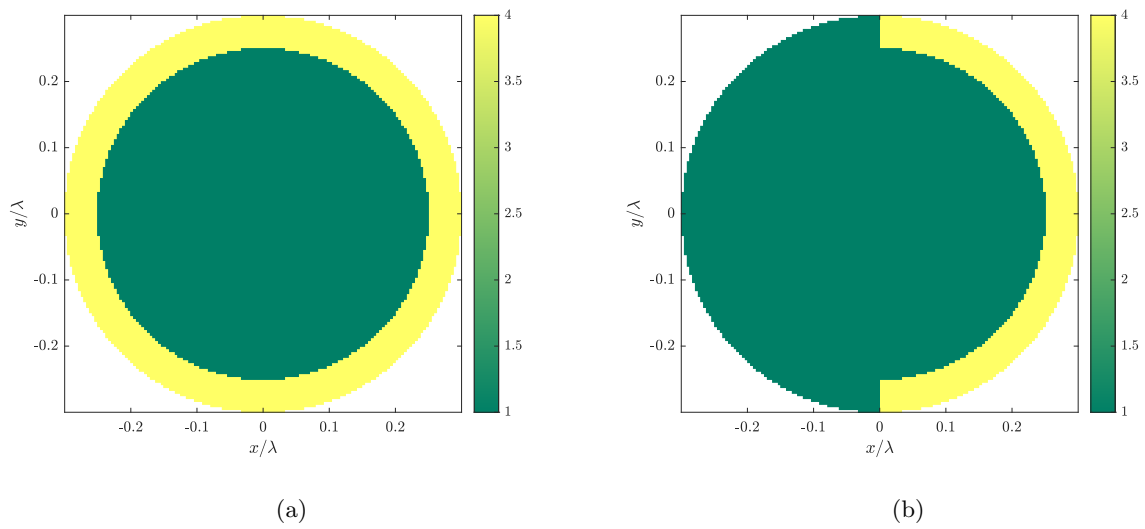


Figure 21: Relative permittivity distribution: (a) a circular shell: the outer radius is  $0.3\lambda$  and the inner radius is  $0.25\lambda$ ; (b) a semi-circular shell.

## Appendix B (Continued)

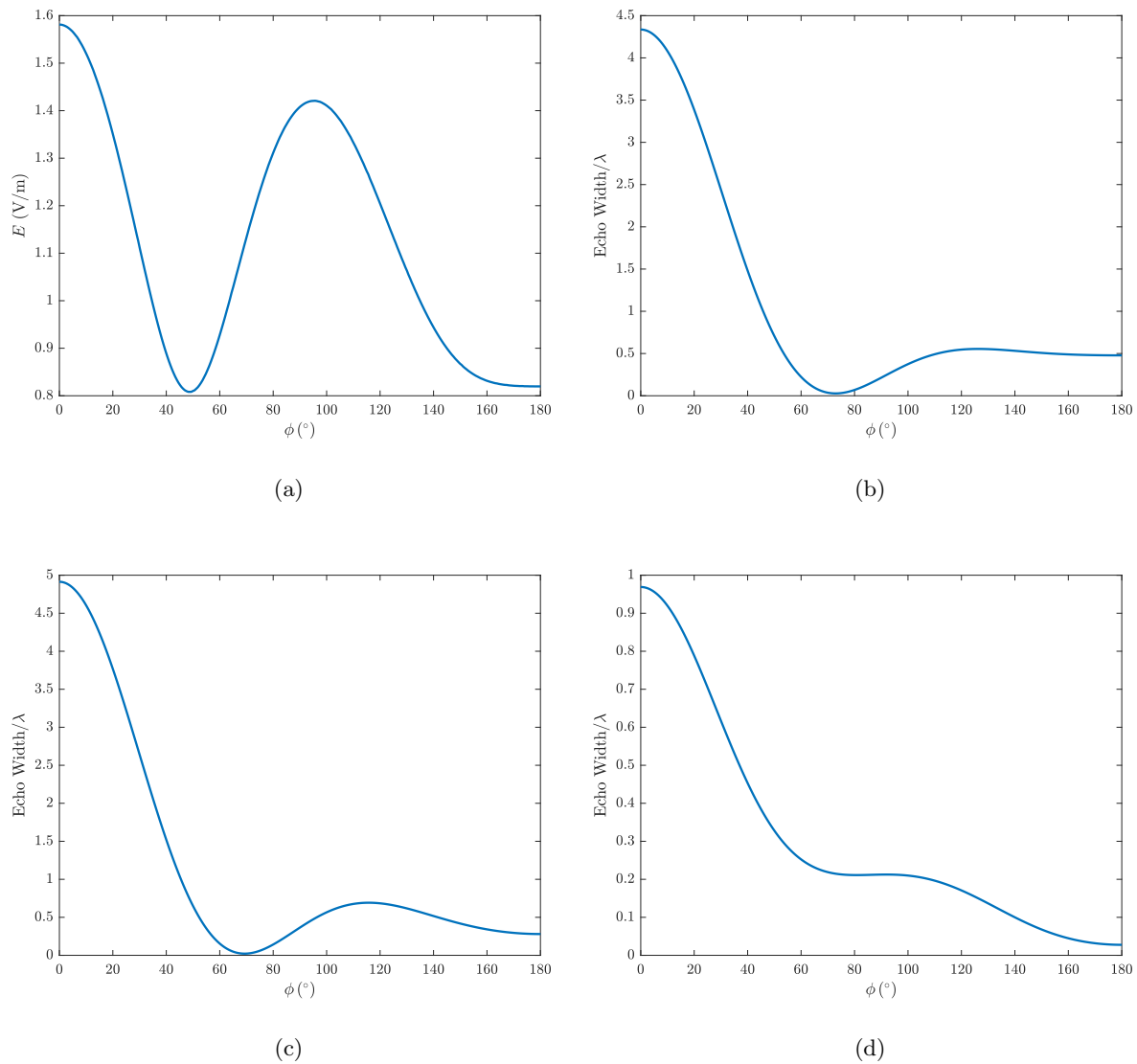


Figure 22: MoM solver results for Figure 21a: (a) electric field in the shell along the radius of  $0.275\lambda$ ; (b) echo width with a plane wave incident; (c) echo width with a line source incident. MoM solver results for Figure 21b: (d) echo width with a plane wave incident.

## Appendix C

### COPYRIGHT PERMISSION: DISSERTATION REUSE

This Appendix includes the copyright permission to reuse IEEE material from Copyright Clearance Center RightsLink<sup>®</sup>.

**The IEEE does not require individuals working on a thesis to obtain a formal reuse license, however, you may print out this statement to be used as a permission grant:**

*Requirements to be followed when using any portion (e.g., figure, graph, table, or textual material) of an IEEE copyrighted paper in a thesis:*

1) In the case of textual material (e.g., using short quotes or referring to the work within these papers) users must give full credit to the original source (author, paper, publication) followed by the IEEE copyright line © 2011 IEEE.

2) In the case of illustrations or tabular material, we require that the copyright line © [Year of original publication] IEEE appear prominently with each reprinted figure and/or table.

3) If a substantial portion of the original paper is to be used, and if you are not the senior author, also obtain the senior author's approval.

*Requirements to be followed when using an entire IEEE copyrighted paper in a thesis:*

1) The following IEEE copyright/ credit notice should be placed prominently in the references: © [year of original publication] IEEE. Reprinted, with permission, from [author names, paper title, IEEE publication title, and month/year of publication]

## Appendix C (Continued)

2) Only the accepted version of an IEEE copyrighted paper can be used when posting the paper or your thesis on-line.

3) In placing the thesis on the author's university website, please display the following message in a prominent place on the website: In reference to IEEE copyrighted material which is used with permission in this thesis, the IEEE does not endorse any of [university/educational entity's name goes here]'s products or services. Internal or personal use of this material is permitted. If interested in reprinting/republishing IEEE copyrighted material for advertising or promotional purposes or for creating new collective works for resale or redistribution, please go to [http://www.ieee.org/publications\\_standards/publications/rights/rights\\_link.html](http://www.ieee.org/publications_standards/publications/rights/rights_link.html) to learn how to obtain a License from RightsLink.

If applicable, University Microfilms and/or ProQuest Library, or the Archives of Canada may supply single copies of the dissertation.

## CITED LITERATURE

1. Y. Liu, F. Soldovieri, and D. Erricolo, “A combination of deterministic regularizations and genetic algorithms in two-dimensional inverse scattering problems,” in *2020 43rd International Conference on Telecommunications and Signal Processing (TSP)*, pp. 466–469, 2020.
2. Y. Liu and D. Erricolo, “An application of Monte Carlo Markov chains in inverse electromagnetic scattering problems,” in *2021 XXXIVth General Assembly and Scientific Symposium of the International Union of Radio Science (URSI GASS)*, pp. 1–4, 2021.
3. Y. Liu, S. Han, F. Soldovieri, and D. Erricolo, “An approximation of 2-D inverse scattering problems from a convex optimization perspective,” *IEEE Geoscience and Remote Sensing Letters*, vol. 19, pp. 1–5, 2022.
4. J. Dewitt and E. Stodola, “Detection of radio signals reflected from the moon,” *Proceedings of the IRE*, vol. 37, no. 3, pp. 229–242, 1949.
5. J. V. Evans and G. H. Pettengill, “The scattering behavior of the moon at wavelengths of 3.6, 68, and 784 centimeters,” *Journal of Geophysical Research (1896-1977)*, vol. 68, no. 2, pp. 423–447, 1963.
6. H. J. Moore, J. M. Boyce, G. G. Schaber, and D. H. Scott, “Lunar remote sensing and measurements,” tech. rep., United States Government Printing Office, 1980.
7. J. C. Maxwell, “A dynamical theory of the electromagnetic field,” *Philosophical Transactions of the Royal Society of London*, vol. 155, pp. 459–513, 1865.
8. J. K. Hargreaves, *The Solar-Terrestrial Environment: An Introduction to Geospace - the Science of the Terrestrial Upper Atmosphere, Ionosphere, and Magnetosphere*. Cambridge Atmospheric and Space Science Series, Cambridge University Press, 1992.
9. K. G. Budden, *The Propagation of Radio Waves: The Theory of Radio Waves of Low Power in the Ionosphere and Magnetosphere*. Cambridge University Press, 1985.

10. R. Helliwell, *Whistlers and Related Ionospheric Phenomena*. Stanford University Press, 1965.
11. J. L. Burch, *Image Mission Overview*, pp. 1–14. Dordrecht: Springer Netherlands, 2000.
12. M. A. Richards, ed., *Principles of Modern Radar: Basic principles*. Radar, Sonar & Navigation, Institution of Engineering and Technology, 2010.
13. D. E. Dudgeon and R. M. Mersereau, *Multidimensional Digital Signal Processing*. Prentice Hall Professional Technical Reference, 1990.
14. R. N. Bracewell, “Strip integration in radio astronomy,” *Australian Journal of Physics*, vol. 9, no. 2, pp. 198–217, 1956.
15. R. M. Mersereau and A. V. Oppenheim, “Digital reconstruction of multidimensional signals from their projections,” *Proceedings of the IEEE*, vol. 62, no. 10, pp. 1319–1338, 1974.
16. A. Devaney, *Mathematical Foundations of Imaging, Tomography and Wavefield Inversion*. Cambridge University Press, 2012.
17. M. Pastorino, *Microwave Imaging*. Wiley Series in Microwave and Optical Engineering, Wiley, 2010.
18. R. Solimene, I. Catapano, G. Gennarelli, A. Cuccaro, A. Dell’Aversano, and F. Soldovieri, “SAR imaging algorithms and some unconventional applications: A unified mathematical overview,” *IEEE Signal Processing Magazine*, vol. 31, no. 4, pp. 90–98, 2014.
19. O. Büyüköztürk and H. C. Rhim, “Radar imaging of concrete specimens for non-destructive testing,” *Construction and Building Materials*, vol. 11, no. 3, pp. 195–198, 1997. Investigation of Materials.
20. K. Langenberg, K. Mayer, and R. Marklein, “Nondestructive testing of concrete with electromagnetic and elastic waves: Modeling and imaging,” *Cement and Concrete Composites*, vol. 28, no. 4, pp. 370–383, 2006. Non-Destructive Testing.
21. A. Heifetz, M. Strow, Y. Liu, P. Bevington, P. Zapol, S. Bakhtiari, and A. Bentivegna, “Monitoring of dielectric permittivity in accelerated alkali-silica reaction concrete with microwave backscattering,” *Materials and Structures*, vol. 53, p. 130, Oct 2020.

22. F. Soldovieri and R. Solimene, *Ground Penetrating Radar Subsurface Imaging of Buried Objects*. INTECH Open Access Publisher, 2010.
23. L. L. Monte, F. Soldovieri, D. Erricolo, and M. Wicks, "Radio frequency tomography for below ground imaging and surveillance of targets under cover," in *Effective Surveillance for Homeland Security: Balancing Technology and Social Issues* (F. Flammini, R. Setola, and G. Franceschetti, eds.), Taylor & Francis/CRC Press, 2013.
24. L. Lo Monte, D. Erricolo, F. Soldovieri, and M. C. Wicks, "Radio frequency tomography for tunnel detection," *IEEE Transactions on Geoscience and Remote Sensing*, vol. 48, no. 3, pp. 1128–1137, 2010.
25. F. Soldovieri, L. L. Monte, and D. Erricolo, "Tunnel detection and localization via multi-monostatic RF tomography using magnetic sources," *IET Radar, Sonar & Navigation*, vol. 6, pp. 834–845, Dec. 2012.
26. L. Lo Monte, D. Erricolo, F. Soldovieri, and M. Wicks, "RF tomography for below-ground imaging of extended areas and close-in sensing," *IEEE Geoscience and Remote Sensing Letters*, vol. 7, pp. 496–500, July 2010.
27. L. L. Monte, F. Soldovieri, D. Erricolo, and M. Wicks, "Imaging below irregular terrain using RF tomography," *IEEE Transactions on Geoscience and Remote Sensing*, vol. 50, pp. 3364–3373, Sept. 2012.
28. L. L. Monte, F. Soldovieri, D. Erricolo, A. Giannopoulos, and M. C. Wicks, "A comprehensive forward model for imaging under irregular terrain using RF tomography," *International Journal of Antennas and Propagation, Special Issue on Propagation Models and Inversion Approaches for Subsurface and Through-Wall Imaging*, vol. 2012, 2012. doi:10.1155/2012/735414.
29. J. Goswami, R. Mydur, P. Wu, and D. Heliot, "A robust technique for well-log data inversion," *IEEE Transactions on Antennas and Propagation*, vol. 52, no. 3, pp. 717–724, 2004.
30. L. Li, L. G. Wang, F. L. Teixeira, C. Liu, A. Nehorai, and T. J. Cui, "DeepNIS: Deep neural network for nonlinear electromagnetic inverse scattering," *IEEE Transactions on Antennas and Propagation*, vol. 67, no. 3, pp. 1819–1825, 2019.

31. R. Scapaticci, P. Kosmas, and L. Crocco, "Wavelet-based regularization for robust microwave imaging in medical applications," *IEEE Transactions on Biomedical Engineering*, vol. 62, no. 4, pp. 1195–1202, 2015.
32. C. A. Balanis, *Advanced Engineering Electromagnetics, 2nd Edition*. Wiley, 2012.
33. C. A. Balanis, *Antenna Theory: Analysis and Design*. Wiley, 2016.
34. P. Uslenghi, *Electromagnetic Scattering*. Elsevier Science, 2012.
35. J. J. Bowman, T. B. A. Senior, and P. L. E. Uslenghi, *Electromagnetic and Acoustic Scattering by Simple Shapes*. New York: Hemisphere Publishing Corporation, 1987.
36. M. Bertero, P. Boccacci, and C. De Mol, *Introduction to Inverse Problems in Imaging*. CRC Press, 2021.
37. M. Ambrosanio, M. T. Bevacqua, T. Isernia, and V. Pascazio, "The tomographic approach to ground-penetrating radar for underground exploration and monitoring: A more user-friendly and unconventional method for subsurface investigation," *IEEE Signal Processing Magazine*, vol. 36, no. 4, pp. 62–73, 2019.
38. R. F. Harrington, *Field Computation by Moment Methods*. Wiley-IEEE Press, 1993.
39. J. Jin, *The Finite Element Method in Electromagnetics*. IEEE Press, Wiley, 2015.
40. T. M. Habashy, R. W. Groom, and B. R. Spies, "Beyond the Born and Rytov approximations: A nonlinear approach to electromagnetic scattering," *Journal of Geophysical Research: Solid Earth*, vol. 98, no. B2, pp. 1759–1775, 1993.
41. D. Wolpert and W. Macready, "No free lunch theorems for optimization," *IEEE Transactions on Evolutionary Computation*, vol. 1, no. 1, pp. 67–82, 1997.
42. R. Pierri, F. Soldovieri, A. Liseno, and F. De Blasio, "Dielectric profiles reconstruction via the quadratic approach in 2-D geometry from multifrequency and multifrequency/multiview data," *IEEE Transactions on Geoscience and Remote Sensing*, vol. 40, no. 12, pp. 2709–2718, 2002.
43. G. Oliveri, N. Anselmi, and A. Massa, "Compressive sensing imaging of non-sparse 2D scatterers by a total-variation approach within the Born approximation," *IEEE Transactions on Antennas and Propagation*, vol. 62, no. 10, pp. 5157–5170, 2014.

44. T. Negishi, V. Picco, L. L. Monte, and D. Erricolo, "Dyadic contrast function for the forward model of diffraction tomography of thin cylindrical objects," *IEEE Antennas and Wireless Propagation Letters*, vol. 16, pp. 991–994, 2017.
45. P. Morse and H. Feshbach, *Methods of Theoretical Physics*. International series in pure and applied physics, McGraw-Hill, 1953.
46. M. Born, E. Wolf, A. B. Bhatia, P. C. Clemmow, D. Gabor, A. R. Stokes, A. M. Taylor, P. A. Wayman, and W. L. Wilcock, *Principles of Optics: Electromagnetic Theory of Propagation, Interference and Diffraction of Light*. Cambridge University Press, 7 ed., 1999.
47. F. Natterer, "An error bound for the Born approximation," *Inverse Problems*, vol. 20, pp. 447–452, jan 2004.
48. V. Picco, G. Gennarelli, T. Negishi, F. Soldovieri, and D. Erricolo, "Experimental validation of the quadratic forward model for rf tomography," *IEEE Geoscience and Remote Sensing Letters*, vol. 12, no. 7, pp. 1461–1465, 2015.
49. Guozhong Gao and C. Torres-Verdin, "High-order generalized extended Born approximation for electromagnetic scattering," *IEEE Transactions on Antennas and Propagation*, vol. 54, no. 4, pp. 1243–1256, 2006.
50. A. J. Devaney, "Inverse-scattering theory within the Rytov approximation," *Optics Letters*, vol. 6, pp. 374–376, Aug. 1981.
51. R. Pierri, A. Liseno, and F. Soldovieri, "Shape reconstruction from PO multifrequency scattered fields via the singular value decomposition approach," *IEEE Transactions on Antennas and Propagation*, vol. 49, pp. 1333–1343, Sep. 2001.
52. Y. M. Wang and W. C. Chew, "An iterative solution of the two-dimensional electromagnetic inverse scattering problem," *International Journal of Imaging Systems and Technology*, vol. 1, no. 1, pp. 100–108, 1989.
53. W. C. Chew and Y. M. Wang, "Reconstruction of two-dimensional permittivity distribution using the distorted Born iterative method," *IEEE Transactions on Medical Imaging*, vol. 9, pp. 218–225, June 1990.
54. R. F. Remis and P. M. van den Berg, "On the equivalence of the Newton-Kantorovich and distorted Born methods," *Inverse Problems*, vol. 16, no. 1, p. L1, 2000.

55. A. Roger, "Newton-kantorovitch algorithm applied to an electromagnetic inverse problem," *IEEE Transactions on Antennas and Propagation*, vol. 29, no. 2, pp. 232–238, 1981.
56. M. Hidayetoğlu, Chunxia Yang, Lang Wang, A. Podkowa, M. Oelze, Wen-Mei Hwu, and W. C. Chew, "Parallel solutions of inverse multiple scattering problems with Born-type fast solvers," in *2016 Progress in Electromagnetic Research Symposium (PIERS)*, pp. 916–920, Aug 2016.
57. S. Twomey, *Introduction to the Mathematics of Inversion in Remote Sensing and Indirect Measurements*. Developments in geomathematics, Dover Publications, 1996.
58. P. Shah, U. K. Khankhoje, and M. Moghaddam, "Inverse scattering using a joint  $L_1 - L_2$  norm-based regularization," *IEEE Transactions on Antennas and Propagation*, vol. 64, pp. 1373–1384, April 2016.
59. P. M. V. D. Berg and A. Abubakar, "Contrast source inversion method: State of art," in *Progress In Electromagnetics Research*, 34:189–218, 2001.
60. A. Tikhonov and V. Arsenin, *Solutions of ill-posed problems*. Scripta series in mathematics, Winston, 1977.
61. T. Negishi, G. Gennarelli, F. Soldovieri, Y. Liu, and D. Erricolo, "Radio frequency tomography for nondestructive testing of pillars," *IEEE Transactions on Geoscience and Remote Sensing*, vol. 58, no. 6, pp. 3916–3926, 2020.
62. H. Harada, D. J. N. Wall, T. Takenaka, and M. Tanaka, "Conjugate gradient method applied to inverse scattering problem," *IEEE Transactions on Antennas and Propagation*, vol. 43, no. 8, pp. 784–792, 1995.
63. P. Joly and G. Meurant, "Complex conjugate gradient methods," *Numerical Algorithms*, vol. 4, pp. 379–406, Oct 1993.
64. L. N. de Castro, "Fundamentals of natural computing: an overview," *Physics of Life Reviews*, vol. 4, no. 1, pp. 1–36, 2007.
65. Y. Rahmat-Samii and E. Michielssen, *Electromagnetic Optimization by Genetic Algorithms*. Wiley Series in Microwave and Optical Engineering, Wiley, 1999.
66. R. L. Haupt, "An introduction to genetic algorithms for electromagnetics," *IEEE Antennas and Propagation Magazine*, vol. 37, no. 2, pp. 7–15, 1995.

67. G. Hornby, A. Globus, D. Linden, and J. Lohn, "Automated antenna design with evolutionary algorithms," in *Space 2006*, p. 7242, 2006.
68. S. Caorsi, A. Massa, and M. Pastorino, "A crack identification microwave procedure based on a genetic algorithm for nondestructive testing," *IEEE Transactions on Antennas and Propagation*, vol. 49, no. 12, pp. 1812–1820, 2001.
69. S. Caorsi, A. Massa, M. Pastorino, and A. Randazzo, "Electromagnetic detection of dielectric scatterers using phaseless synthetic and real data and the memetic algorithm," *IEEE Transactions on Geoscience and Remote Sensing*, vol. 41, no. 12, pp. 2745–2753, 2003.
70. M. Salucci, L. Poli, N. Anselmi, and A. Massa, "Multifrequency particle swarm optimization for enhanced multiresolution gpr microwave imaging," *IEEE Transactions on Geoscience and Remote Sensing*, vol. 55, no. 3, pp. 1305–1317, 2017.
71. N. Meuleau and M. Dorigo, "Ant colony optimization and stochastic gradient descent," *Artificial Life*, vol. 8, no. 2, pp. 103–121, 2002.
72. S. Naka, T. Genji, T. Yura, and Y. Fukuyama, "A hybrid particle swarm optimization for distribution state estimation," *IEEE Transactions on Power systems*, vol. 18, no. 1, pp. 60–68, 2003.
73. R. Poli, C. Di Chio, and W. B. Langdon, "Exploring extended particle swarms: a genetic programming approach," in *Proceedings of the 7th annual conference on Genetic and evolutionary computation*, pp. 169–176, ACM, 2005.
74. S. Caorsi, A. Massa, and M. Pastorino, "A computational technique based on a real-coded genetic algorithm for microwave imaging purposes," *IEEE Transactions on Geoscience and Remote Sensing*, vol. 38, pp. 1697–1708, July 2000.
75. A. Tarantola, *Inverse Problem Theory and Methods for Model Parameter Estimation*. Other Titles in Applied Mathematics, Society for Industrial and Applied Mathematics, 2005.
76. J. Richmond, "Scattering by a dielectric cylinder of arbitrary cross section shape," *IEEE Transactions on Antennas and Propagation*, vol. 13, pp. 334–341, May 1965.

77. J. P. Kaipio, V. Kolehmainen, E. Somersalo, and M. Vauhkonen, “Statistical inversion and Monte Carlo sampling methods in electrical impedance tomography,” *Inverse Problems*, vol. 16, pp. 1487–1522, oct 2000.
78. S. Boyd and L. Vandenberghe, *Convex Optimization*. USA: Cambridge University Press, 2004.
79. J. Goswami and A. Chan, *Fundamentals of Wavelets: Theory, Algorithms, and Applications*. Wiley Series in Microwave and Optical Engineering, Wiley, 2011.
80. M. T. Bevacqua, L. Crocco, L. D. Donato, and T. Isernia, “Non-linear inverse scattering via sparsity regularized contrast source inversion,” *IEEE Transactions on Computational Imaging*, vol. 3, no. 2, pp. 296–304, 2017.
81. N. Anselmi, M. Salucci, G. Oliveri, and A. Massa, “Wavelet-based compressive imaging of sparse targets,” *IEEE Transactions on Antennas and Propagation*, vol. 63, no. 11, pp. 4889–4900, 2015.
82. A. Abubakar, T. M. Habashy, Y. Lin, and M. Li, “A model-compression scheme for non-linear electromagnetic inversions,” *Geophysics*, vol. 77, pp. E379–E389, Sept. 2012.
83. H. Mittelmann, “Benchmarks for Optimization Software.” <http://plato.asu.edu/bench.html>.
84. M. Grant and S. Boyd, “CVX: Matlab software for disciplined convex programming, version 2.1.” <http://cvxr.com/cvx>, Mar. 2014.
85. M. Grant and S. Boyd, “Graph implementations for nonsmooth convex programs,” in *Recent Advances in Learning and Control* (V. Blondel, S. Boyd, and H. Kimura, eds.), Lecture Notes in Control and Information Sciences, pp. 95–110, Springer-Verlag Limited, 2008.
86. S. J. Wright, *Primal-Dual Interior-Point Methods*. SIAM, 1997.
87. R. Tibshirani, “Regression shrinkage and selection via the Lasso,” *Journal of the Royal Statistical Society. Series B (Methodological)*, vol. 58, no. 1, pp. 267–288, 1996.
88. S. R. Becker, E. J. Candès, and M. C. Grant, “Templates for convex cone problems with applications to sparse signal recovery,” *Mathematical Programming Computation*, vol. 3, no. 3, p. 165, 2011.

89. A. J. Devaney, "Fundamental limitations in inverse source and scattering problems in NDE," 1986.
90. W. C. Chew, Y. Wang, G. Otto, D. Lesselier, and J.-C. Bolomey, "On the inverse source method of solving inverse scattering problems," *Inverse Problems*, vol. 10, no. 3, p. 547, 1994.
91. V. Picco, T. Negishi, S. Nishikata, D. Spitzer, and D. Erricolo, "RF tomography in free space: experimental validation of the forward model and an inversion algorithm based on the algebraic reconstruction technique," *International Journal of Antennas and Propagation*, 2013. Article ID 528347, doi:10.1155/2013/528347.
92. W. C. Chew, Y. M. Wang, G. Otto, D. Lesselier, and J. C. Bolomey, "On the inverse source method of solving inverse scattering problems," *Inverse Problems*, vol. 10, pp. 547–553, June 1994.
93. J. D. Lee, Y. Sun, and M. A. Saunders, "Proximal newton-type methods for minimizing composite functions," *SIAM Journal on Optimization*, vol. 24, no. 3, pp. 1420–1443, 2014.
94. J. D. Lee, Y. Sun, and M. Saunders, "Proximal newton-type methods for convex optimization," in *Advances in Neural Information Processing Systems* (F. Pereira, C. J. C. Burges, L. Bottou, and K. Q. Weinberger, eds.), vol. 25, Curran Associates, Inc., 2012.
95. C. Tai, I. Antennas, P. Society, I. M. Theory, and T. Society, *Dyadic Green Functions in Electromagnetic Theory*. IEEE Press Publication Series, IEEE Press, 1994.

## VITA

Yangqing Liu

EDUCATION	Ph.D., Electrical and Computer Engineering University of Illinois Chicago	2015–2022
	M.E.E., Electrical Engineering University of Alaska Fairbanks	2011–2014
	B.E., Electrical Engineering and Automation Hebei University of Engineering, China	2007–2011
EXPERIENCE	Intern Tesla, Inc.	8/2021–12/2021 Fremont, CA
	Intern ANSYS, Inc.	5/2019–8/2019 Canonsburg, PA
	Research Aide Technical Argonne National Laboratory	6/2017–8/2017 Lemont, IL
	Teaching Assistant University of Illinois Chicago	2016–2021 Chicago, IL
	Teaching Assistant University of Alaska Fairbanks	2011–2014 Fairbanks, AK
	SERVICE	Mentor Army Education Outreach Program
PUBLICATION	<i>Yangqing Liu</i> , Tadahiro Negishi, and Danilo Erricolo, Exact solution of electromagnetic scattering from a dipole antenna located inside a multilayer metamaterial oblate spheroidal cavity, <i>URSI Radio Science Letters</i> , vol. 3, 2021, doi: 10.46620/21-0018.	
	<i>Yangqing Liu</i> and Danilo Erricolo, An application of Monte Carlo Markov chains in inverse electromagnetic scattering problems, <i>URSI GASS 2021</i> , Rome, Italy, Aug. 28–Sep. 24, 2021.	
	<i>Yangqing Liu</i> , Shuo Han, Francesco Soldovieri, and Danilo Erricolo, An approximation of inverse scattering problems: a convex optimization perspective, <i>IEEE Geoscience and Remote Sensing Letters</i> , vol. 19, pp. 1-5, 2022, Art no. 8012305, doi: 10.1109/LGRS.2021.3079885.	

Alexander Heifetz, Meredith Strow, *Yangqing Liu*, Peter Bevington, Peter Zapol, Sasan Bakhtiari, and Anthony Bentivegna, Monitoring of dielectric permittivity in accelerated alkali-silica reaction concrete with microwave backscattering, *Materials and Structures*, 53, 130, 2020.

*Yangqing Liu*, Francesco Soldovieri, and Danilo Erricolo, A combination of deterministic regularizations and genetic algorithms in two-dimensional inverse scattering problems, *43rd International Conference on Telecommunications and Signal Processing*, Milan, Italy, July 7–9, 2020.

Tadahiro Negishi, Gianluca Gennarelli, Francesco Soldovieri, *Yangqing Liu*, and Danilo Erricolo, Radio frequency tomography for nondestructive testing of pillars, *IEEE Transactions on Geoscience and Remote Sensing*, vol. 58, no. 6, pp. 3916-3926, June 2020.

Damien Gilbert, *Yangqing Liu*, and Danilo Erricolo, A planar positioning system for antennas, *USNC-URSI National Radio Science Meeting*, Boulder, CO, Jan. 9–12, 2019.

*Yangqing Liu* and Danilo Erricolo, Ultimate intrinsic signal-to-noise ratio of MRI surface coils for a lossy dielectric elliptical cylinder, *USNC-URSI National Radio Science Meeting*, Boulder, CO, Jan. 4–7, 2018.

Tadahiro Negishi, *Yangqing Liu*, Vittorio Picco, Danilo Erricolo, Gianluca Gennarelli, Francesco Soldovieri, and Piergiorgio L. E. Uslenghi, Experimental validation of radio frequency tomography for an inhomogeneous medium, *URSI Commission B International Symposium on Electromagnetic Theory (EMTS 2016)*, Espoo, Finland, Aug. 14–18, 2016, pp. 5-8.

## PRESENTATION

*Yangqing Liu* and Danilo Erricolo, Two-dimensional inverse scattering using a Bayesian approach, *2019 URSI Commission B International Symposium on Electromagnetic Theory (EMTS 2019)*, San Diego, CA, May 27–31, 2019.

*Yangqing Liu*, Tadahiro Negishi, and Danilo Erricolo, Radio Frequency Tomography for a Reinforced Concrete Cylinder by Genetic Algorithm, *IEEE Antennas and Propagation Society International Symposium/USNC-URSI National Radio Science Meeting*, Boston, MA, July 8–13, 2018.

Tadahiro Negishi, Gianluca Gennarelli, *Yangqing Liu*, Danilo Erricolo, and Francesco Soldovieri, Imaging performance comparison in reinforced concrete pillars using ground penetrating radar and radio frequency tomography, *USNC-URSI National Radio Science Meeting*, Boulder, CO, Jan. 4–7, 2017.

*Yangqing Liu*, Tadahiro Negishi, and Danilo Erricolo, Exact electromagnetic scattering from a dipole antenna located inside a multilayer metamaterial oblate spheroidal cavity, *USNC-URSI National Radio Science Meeting*, Boulder, CO, Jan. 6–9, 2016.

Vikas Sonwalkar, Amani Reddy, Kumar Mayank, Susmita Hazra, *Yangqing Liu*, and Donald Carpenter, Measurement of Field Aligned Electron and Ion Densities and Ducts from the Whistler and Z Mode Radio Sounding from IMAGE, *American Geophysical Union Fall Meeting*, San Francisco, CA, Dec. 9–13, 2013.

Vikas Sonwalkar, Susmita Hazra, Kumar Mayank, Amani Reddy, *Yangqing Liu*, and Donald Carpenter, Whistler and Z Mode Radio Sounding Results from IMAGE: Implications for the Generation and Propagation of Naturally Occurring Plasma Waves, *American Geophysical Union Fall Meeting*, San Francisco, CA, Dec. 3–7, 2012.

MEMBERSHIPS	Institute of Electrical and Electronics Engineers	2015–present
	American Geophysical Union	2012–2014